

Low-Frequency Currents from Deep Moorings in the Southern Bay of Bengal

H. W. WIJESSEKERA, W. J. TEAGUE, D. W. WANG, E. JAROSZ, AND T. G. JENSEN

Naval Research Laboratory, Stennis Space Center, Mississippi

S. U. P. JINADASA

National Aquatic Resources Research and Development Agency, Crow Island, Sri Lanka

H. J. S. FERNANDO

*University of Notre Dame, Department of Civil Engineering, Environmental and Earth Sciences,
Notre Dame, Indiana*

Z. R. HALLOCK

NVision Solutions, Inc., Bay St. Louis, Mississippi

(Manuscript received 6 May 2016, in final form 12 August 2016)

ABSTRACT

High-resolution currents and hydrographic fields were measured at six deep-water moorings in the southern Bay of Bengal (BoB) by the Naval Research Laboratory as part of an international effort focused on the dynamics of the Indian Ocean. Currents, temperature, and salinity were sampled over the upper 500 m for 20 months between December 2013 and August 2015. One of the major goals is to understand the space–time scales of the currents and physical processes that contribute to the exchange of water between the BoB and the Arabian Sea. The observations captured Southwest and Northeast Monsoon Currents, seasonally varying large eddies including a cyclonic eddy, the Sri Lanka dome (SLD), and an anticyclonic eddy southeast of the SLD. The observations further showed intraseasonal oscillations with periods of 30–70 days, near-inertial currents, and tides. Monthly averaged velocities commonly exceeded 50 cm s^{-1} near the surface, and extreme velocities exceeded 150 cm s^{-1} during the southwest monsoon. Tides were small and dominated by the M_2 component with velocities of about 3 cm s^{-1} . The average transport into the BoB over the measurement period was 2 Sv ($1 \text{ Sv} \equiv 10^6 \text{ m}^3 \text{ s}^{-1}$) but likely exceeded 15 Sv during summer of 2014. This study suggests the water exchange away from coastal boundaries, in the interior of the BoB, may be largely influenced by the location and strength of the two eddies that modify the path of the Southwest Monsoon Current. In addition, there is a pathway below 200 m for transport of water into the BoB throughout the year.

1. Introduction

The southern Bay of Bengal, east of Sri Lanka, is an important region for understanding the interaction of currents and water masses from the Bay of Bengal (BoB), Arabian Sea (AS), and the equatorial Indian Ocean. The entire BoB undergoes a dramatic seasonal variation in circulation patterns. Hydrographic observations in the western BoB and near the coast have been

primarily used to document the seasonality (e.g., Shetye et al. 1993; Murty et al. 1992; Shankar et al. 2002). Seasonally reversing north–south currents, such as the East Indian Coastal Current (EICC) near the east coasts of Sri Lanka and India, transport low-salinity water from the BoB into the AS while the overall flows are equatorward (Shetye et al. 1996; Mukherjee et al. 2014). Seasonally reversing east–west monsoon-driven currents pass just south of Sri Lanka and transport water between the southern BoB and AS. The Northeast (NE) Monsoon Current (NMC) flows westward during winter and the Southwest (SW) Monsoon Current (SMC) flows eastward during summer (also known as the Winter Monsoon Current and Summer Monsoon Current,

Corresponding author address: Hemantha W. Wijesekera, Naval Research Laboratory, 1009 Balch Blvd., Stennis Space Center, MS 39529.

E-mail: hemantha.wijesekera@nrlssc.navy.mil

respectively; Schott et al. 1994; Schott and McCreary 2001; Jensen 2001; Vinayachandran et al. 2013). A major influx for saltier water into the BoB originates with the SMC (Murty et al. 1992; Schott et al. 1994; Jensen 2001, 2003; Vinayachandran et al. 2002). Freshwater inputs from rainfall and rivers and shallow, salinity-controlled mixed layers are important factors and have a strong influence in the flushing of the BoB (Shenoi et al. 2002).

Air–sea interaction and monsoon variability have been the focus of several earlier field experiments (e.g., Bhat et al. 2001; Murty et al. 1996; Webster et al. 2002; Rao et al. 2011). The Bay of Bengal Monsoon Experiment (BOBMEX) examined organized convection during July–August 1999 (Bhat et al. 2001). Webster et al. (2002) addressed intraseasonal and interannual variability of the monsoon in the eastern Indian Ocean spanning 5°S to 15°N as part of the Joint Air–Sea Monsoon Interaction Experiment (JASMINE). Rao et al. (2011) examined intraseasonal variability and monsoon break cycles in the northern BoB during July–August 2009 during the continental tropical convergence zone (CTCZ) program. Although these studies contributed to the understanding of the ocean–atmospheric processes in the BoB, there have been only a few studies where subsurface currents have been directly measured. The SMC and NMC currents were first measured by Schott et al. (1994) south of Sri Lanka using long-term moorings equipped with acoustic Doppler current profilers (ADCPs) and snapshots from a shipboard ADCP. During the winter monsoon, they observed a westward-flowing NMC, which had a mean transport of about 12 Sv ($1 \text{ Sv} \equiv 10^6 \text{ m}^3 \text{ s}^{-1}$), while during the summer monsoon, the eastward-flowing SMC carried a transport of about 8 Sv for the region north of 3.75°N. The currents east of Sri Lanka in the deep water in the southern BoB have never been measured by long-term fixed moorings. Drifters, satellite altimetry, hydrography, and shipboard ADCPs (e.g., Shetye et al. 1996; Hacker et al. 1998; Vinayachandran et al. 1999; Wijesekera et al. 2015) have provided clues regarding the near-surface circulation. Recent shipboard and surface drifter observations have revealed that low-salinity water was transported out of the BoB by the EICC and that high-salinity water was transported into the BoB by a northward, subsurface-intensified flow east of the EICC (Wijesekera et al. 2015). Westerly wind bursts over the equatorial Indian Ocean have been suggested to be important in determining the saltwater intrusions in the southern BoB during the northeast monsoon (Wijesekera et al. 2015). Details of the current variability and upper-ocean processes, particularly in the upper several hundred meters, and exchange pathways are not well established, although it is believed that a

regional meridional circulation exchanges water between the BoB and Indian Ocean across the equator (Schott et al. 2002). The seasonal cycle of the circulation and its structure is certainly not clear in the interior of the BoB (Vinayachandran and Yamagata 1998).

During the field program for Effects of Bay of Bengal Freshwater Flux on Indian Ocean Monsoon (EBoB) conducted by the U.S. Naval Research Laboratory (NRL), six deep-water moorings were deployed for a period of 20 months in the south-central BoB. The moorings were located in a transition region in which the dynamics are influenced by the low-salinity northern BoB flow field and the high-salinity equatorial flows in the southern Arabian Sea. Furthermore, the moorings were located in the path of tidal beams that radiate from shallow gaps between the Andaman and Nicobar Islands. This program was part of an international effort by the Air–Sea Interactions in Northern Indian Ocean (ASIRI) of the U.S. Office of Naval Research, the Ocean Mixing and Monsoons (OMM) of the Monsoon Mission of India, and the Coastal Current Observations Program (CCOP) of Sri Lanka (Lucas et al. 2014; Wijesekera et al. 2016b; <http://tos.org/oceanography/issue/volume-29-issue-02>). A major focus of the EBoB observations was to understand the fresh and saltwater exchanges between the BoB and the Arabian Sea. Long-term in situ observations of subsurface currents and hydrographic fields obtained by EBoB are being used to understand the mesoscale to small-scale dynamics and to assess the water mass exchanges on seasonal to sub-seasonal time scales. To our knowledge, the EBoB moorings are the first and so far the only long-term ADCP moorings to be deployed in the south-central BoB that provided current profiles of the upper 500 m of the water column.

Here, we provide the basic description of the dataset while focusing on seasonal and intraseasonal to tidal frequencies to set the stage for later research on specific dynamical processes. In addition, the observed currents will be used to assess the pathways of salt and heat exchanges in the southern BoB. The current structure and variability over the upper 500 m of the water column at water depths of nearly 4000 m are examined in detail. Measurements captured currents in the Sri Lanka dome (de Vos et al. 2014; Vinayachandran and Yamagata 1998) and in a large anticyclonic eddy that often appeared south of the dome (Schott et al. 1994; Vinayachandran et al. 1999). We examine the dominant periods of current variability and put the currents in geographic perspective using sea surface height fields from satellite altimetry.

The paper mainly discusses the seasonal to intra-seasonal current variability, eddies, and possible water

TABLE 1. ADCP mooring summary; 300-kHz ADCP was upward looking and 75-kHz ADCP was downward looking. Z_{buoy} is the depth of the top buoy or the ADCP ball. H is the water depth. Δt is the sampling period of ADCPs. Z_1 , Z_n , and Z_b are the depth of the first bin, the depth of the last bin, and the bin size, respectively. All depths are in meters. T_f is the inertial period in days. Start day and end day are given as day and month for 2013 and 2015, respectively. The site locations of NRL1–6 are marked in triangles in Fig. 1.

Site	Lat ($^{\circ}$ N)	Lon ($^{\circ}$ E)	Start day	End day	Δt (min)	Z_1 (m)	Z_n (m)	Z_b (m)	Z_{buoy} (m)	H (m)	Type (kHz)	T_f (days)
NRL1	5.009	85.511	19 Dec	6 Aug	30	6	134	2	44	3715	300	5.711
			19 Dec	6 Aug	60	64	592	8			75	
NRL2	6.500	85.500	19 Dec	7 Aug	30	6	106	2	39	3876	300	4.405
			19 Dec	7 Aug	60	56	768	8			75	
NRL3	8.000	85.500	20 Dec	8 Aug	30	6	126	2	16	3757	300	3.583
			20 Dec	8 Aug	60	32	592	8			75	
NRL4	7.992	86.990	21 Dec	9 Aug	30	6	142	2	45	3678	300	3.586
			21 Dec	9 Aug	60	64	576	8			75	
NRL5	7.983	88.500	21 Dec	10 Aug	30	6	166	2	72	3638	300	3.590
			21 Dec	10 Aug	60	88	624	8			75	
NRL6	6.500	87.000	22 Dec	11 Aug	30	6	112	2	59	3840	300	4.405
			22 Dec	11 Aug	60	80	576	8			75	

exchange pathways. The paper is organized as follows: The moorings and data are described in section 2. Background winds and sea surface heights are described in sections 3 and 4, respectively. Statistics of the seasonal currents are given in section 5. In section 6, multiple scales, such as tidal, inertial, and subseasonal variability of currents and temperature, are identified from wavelet and conventional spectral methods. Monthly current variability is discussed in section 7. Descriptions of the currents and eddies are given in section 8. Transports are discussed in section 9. Discussions of currents, transport estimates, and comparison with past studies are given in section 10. Summary and conclusions of this study are presented in section 11.

2. Instrumentation and moored datasets

Six ADCP moorings were deployed in a triangular array in the south-central BoB at water depths of nearly 4000 m for a period of about 20 months. These moorings were designed to capture lateral gradients of currents and hydrography, and high-resolution seasonal and intraseasonal currents, eddies, internal waves, and tides originating from the Andaman–Nicobar Island gaps. Locations of the moorings (Table 1) and the bathymetry are shown in Fig. 1. The moorings, located about 200 nm east of Sri Lanka, were about 90 nm (165 km) apart in north–south (meridional) and east–west (zonal) lines. The moorings were deployed in December 2013 and were recovered in August 2015. Both mooring efforts used the R/V *Roger Revelle* operating out of the port of Colombo, Sri Lanka. Each mooring contained an upward-looking Teledyne RD Instruments Workhorse ADCP, operating at 300 kHz, and a downward-looking Teledyne RD Instruments Long Ranger ADCP,

operating at 75 kHz, that were mounted at the top of the mooring in a Flotation Technology buoy, 45 in. in diameter, at a planned depth of 75 m. Nevertheless, the actual buoy depths after deployment were from about 16 to 72 m. Additional flotation was provided by a large ball, 36 in. in diameter, that was located 500 m below the top buoy, and by five sets of four glass balls, 17 in. in

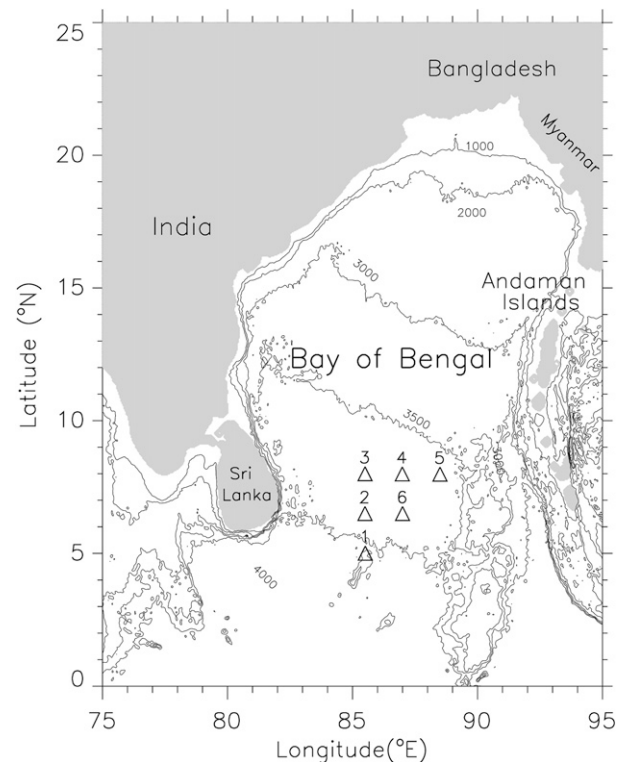


FIG. 1. Bathymetric map of the BoB. Locations of the moorings are marked by triangles.

TABLE 2. String mooring summary. Depth in meters below the top of the ADCP buoy is Δz for NRL moorings 1–6; SCTD indicates the Star Oddi CTD (10-min sampling); *T* indicates the Vemco temperature recorder (1 min); MCP indicates the Microcat temperature and conductivity with pressure recorder (10 min); MC indicates the Microcat temperature and conductivity recorder (10 min); AT indicates the Aqua Troll temperature, conductivity, and pressure recorder (10 min); and C Pod (χ pod) indicates the pressure, temperature, and acceleration recorder (100 Hz).

Δz (m)	NRL1	NRL2	NRL3	NRL4	NRL5	NRL6
0	SCTD	<i>T</i>	SCTD	SCTD	SCTD	SCTD
1.5						
2	<i>T</i>	AT, <i>T</i>	<i>T</i>	<i>T</i>	<i>T</i>	<i>T</i>
7	MCP	MCP	MCP	MCP	MCP	MCP
12	C Pod	<i>T</i>				
17	<i>T</i>	<i>T</i>	<i>T</i>	<i>T</i>	<i>T</i>	<i>T</i>
22	MC	MC	MC	MC	MC	MC
27	<i>T</i>	<i>T</i>	<i>T</i>	<i>T</i>	<i>T</i>	<i>T</i>
32	C Pod	<i>T</i>				
37	MCP	MCP	MCP	MCP	MCP	MCP
42	<i>T</i>	<i>T</i>	<i>T</i>	<i>T</i>	<i>T</i>	<i>T</i>
47	<i>T</i>	<i>T</i>	<i>T</i>	<i>T</i>	<i>T</i>	<i>T</i>
52	MC	MC	MC	MC	MC	MC
62		<i>T</i>	<i>T</i>	<i>T</i>	<i>T</i>	<i>T</i>
72	<i>T</i>	<i>T</i>	AT, <i>T</i>	AT, <i>T</i>	AT, <i>T</i>	<i>T</i>
102	AT, <i>T</i>	AT, <i>T</i>	<i>T</i>	AT, <i>T</i>	AT, <i>T</i>	<i>T</i>
152	<i>T</i>	<i>T</i>		<i>T</i>	<i>T</i>	<i>T</i>
202	<i>T</i>	<i>T</i>	<i>T</i>	<i>T</i>	<i>T</i>	<i>T</i>
252	<i>T</i>	<i>T</i>	<i>T</i>	<i>T</i>	<i>T</i>	<i>T</i>
302	<i>T</i>	<i>T</i>	<i>T</i>	<i>T</i>	<i>T</i>	<i>T</i>
352	SCTD	SCTD	MC	MC	MC	MC

diameter, spaced about 500 m apart along the mooring line. Jacketed steel wire (0.25 in. in diameter) was used for the upper 2000 m of the mooring line and synthetic rope (0.25 in. in diameter) was used for the mooring line below the wire. The moorings were anchored to the bottom with 3500-lb anchors at water depths between 3600 and 3900 m. A pair of acoustic releases was positioned just above the anchor.

In addition, each mooring contained an assortment of sensors mounted along the wire beneath the ADCP buoy: 12 to 14 temperature (*T*) sensors, 3 to 4 temperature, conductivity (TC) sensors, 4 to 6 temperature, conductivity, and pressure (TCP) sensors, and 2 turbulent sensors. The instruments consisted of MicroCats manufactured by Sea Bird Electronics, both with and without pressure to record the temperature and conductivity; Vemco temperature dataloggers; Aqua Troll conductivity–temperature–depth (CTD) loggers; Star Oddi CTD loggers; and χ pods (Moum and Nash 2009) that record temperature, pressure, and acceleration for determination of temperature variance dissipation rate. Sampling rates were 1 min for the Vemco recorders and 10 min for the other recorders with the exception of the

χ pods, which recorded at 100 Hz for nearly the entire deployment period. These sensors were unevenly spaced and were more numerous within about 70 m of the buoy, where strong stratification was expected. A summary of these recorders are provided in Table 2. The depth difference Δz for each instrument relative to the ADCP buoy is also provided in Table 2.

Current profiles were measured from approximately 5 m below the surface to depths of 600 m. Currents were sampled every hour by the Long Ranger and every half-hour by the Workhorse. Vertical depth resolutions for the current measurements were 8 m for the Long Ranger and 2 m for the Workhorse. The accuracy of the Workhorse is 0.5% of the water velocity $\pm 0.5 \text{ cm s}^{-1}$. Inherent to the ADCP design, interference of the side lobes of the acoustic beams with the main lobes prevented accurate velocity determinations near the surface (~ 5 m). Current velocities were not recorded for about 21 m of the profile due to the blanking zones and vertical bin sizes. The first realizable currents near the buoy were at about 4 m (upward) from the Workhorse and 16 m (downward) from the Long Ranger. The accuracy of the Long Ranger is 1% of the water velocity. Details of the moorings in regards to the ADCP locations, record lengths, sample depths, sample intervals, water depths, instrument type, and the minimum buoy depths are provided in Table 1.

All of the moorings were subjected to motions at semidiurnal tidal frequencies that were enhanced during strong current flows. Pressure records for each mooring show tidally induced dips of a meter or two throughout the deployment. Larger excursions from the minimum buoy depth that ranged from about 10 to 50 m commonly occurred at all of the moorings throughout the measurement period. The larger excursions generally occurred during the summer monsoon periods and when currents were stronger. These excursions do not necessarily correlate with the winds. During the strongest current events, dips of up to about 80 m occurred. The mooring motion was further complicated by fishing activity since the ADCP balls at the tops of the moorings ranged from 16 to 72 m beneath the surface and were often entangled with fishing gear. Evidence of fishing activity was found upon recovery of the moorings at the end of the deployment. Several of the buoys and mooring lines were tangled with large quantities of fishing nets and lines, which could generate extra drag on the mooring lines and cause unexpected displacements. The worst case for fishing impact occurred at NRL2, which dipped from about 50 m to over 250 m over a period of about 15 days. Interestingly, at peak impact, the buoy movement consisted of semidiurnal oscillations with amplitudes over 100 m between depths of about 150 and

300 m for about a week. This large mooring dip did not correspond to a large current or wind event, and therefore fishing activity is the likely cause.

An error analysis was performed on the effects of mooring motion on the measured velocities, and the errors were most pronounced at the semidiurnal period. However, the lateral buoy speeds associated with dipping are only $\sim 1\text{--}2\text{ cm s}^{-1}$, with a few larger bursts and are therefore relatively unimportant. In addition, the buoys were gimballed such that they tilted freely in any direction, in effect enabling the two ADCPs in the buoys to remain vertical even when the mooring lines were tipped. This was corroborated by ADCP recorded tilts, which were small and on the same order as commonly recorded values in other mooring deployments not subject to such extreme mooring motions.

Very little editing was required for the recorded velocity data. Full data records were returned at each mooring with the exception of the Workhorse ADCP at NRL2, which stopped recording after about 10 months, and the Long Ranger ADCP at NRL4, which stopped recording after about 15 months. Data quality was good. The velocity data were gridded using the pressure data and interpolated to common depth levels among the moorings. Many of the analyses here use velocity data that are at 8-m levels. Positive u and v velocity values are eastward and northward, respectively. High-frequency currents at frequencies higher than tidal are not of concern in this paper.

The depths of the sensors attached to the mooring lines were evaluated by interpolating the pressure records of the ADCPs and TCP sensors in conjunction with their known location on the mooring line. The temperatures were then gridded at 4-m depth intervals. Salinity was limited to four to six sensors at each mooring and was not interpolated vertically.

The time series of salinity, temperature, and the east–west velocity component U and the north–south velocity component V as a function of depth are shown for each mooring in Figs. 2–7. The velocities and temperatures were averaged using a 36-h boxcar filter. Hence, there remains inertial streaking in the velocity plots since all the inertial periods at the moorings are greater than 36 h (Table 1). Salinities were pixel plotted and not smoothed since salinity measurements were limited in number and deemed inadequate for proper gridding. In addition, time series of sea surface height anomaly (SSHA) and depth of the 20°C isotherm are shown in Figs. 2–7. The 20°C isotherm depths that were derived from the 10-min and 4-m gridded temperature observations were low-pass filtered over 20 days using a fourth-order Butterworth filter. SSHAs gridded at 0.25° in latitude and 0.25° in longitude at daily intervals were

obtained from the Archiving, Validation, and Interpretation of Satellite Oceanographic Data (AVISO) dataset (available online at <http://www.aviso.altimetry.fr/en/data/products/sea-surface-height-products/global/ssha.html>).

3. Background winds and CTD profiles

Winds were recorded by meteorological sensors mounted at 4 m above the sea surface on several buoys that are part of the Research Moored Array for African–Asian Monsoon Analysis and Prediction (RAMA; McPhaden et al. 2009). The RAMA wind records were not continuous with large data gaps during the experimental period except at 12°N , 90°E . Wind speed and direction at two locations in the BoB and one location at the equator are shown in Fig. 8. The standard 10-m wind speed U_{10} and direction Θ were estimated iteratively by assuming that the near-surface atmospheric boundary layer was near neutral and by using a wind speed–dependent drag coefficient (e.g., Wijesekera et al. 2013). The two RAMA buoys at 12°N , 90°E and 4°N , 90°E are located about 900 and 460 km to the west-northwest of the mooring array, respectively, and the third buoy, at the equator near 80°E , is located about 840 km to the southwest of the mooring array. Gaps in wind records were filled using forecast winds of COAMPS (<http://www.nrlmry.navy.mil/coamps-web/web/home>; Chen et al. 2003), also shown in Fig. 8. Winds measured by shipboard sensors (not shown) during the cruise periods near the moorings and COAMPS products compared well with the average daily wind speed and direction provided by the RAMA buoys. However, the modeled winds at the equator near 80.5°E slightly underestimated the observations (Fig. 8e). The combined COAMPS and RAMA winds provide spatial and temporal variabilities of the winds over the BoB during the experiment. There are significant differences in the winds between the interior of the BoB and the equator near 80°E . SW monsoon (summer monsoon) and NE monsoon (winter monsoon) transitions are quite dramatic, especially in the northern BoB (Figs. 8a,b). However, as expected, the monsoon transitions are modest at the equator (Figs. 8e,f). Inside the BoB, the summer monsoon is clearly defined by the wind direction of about 60° from June through September and the winter monsoon is clearly shown by the wind direction of 240° from November through April. The monsoon transition periods are approximately May and October. The beginning and end of the mooring deployments are within the winter and summer monsoon periods, respectively. The maximum daily averaged wind speed of about 15.5 m s^{-1} was recorded at 12°N , 90°E during the fall transition period in 2014. The mean wind speed was about 6.3 m s^{-1} . Wind speeds were

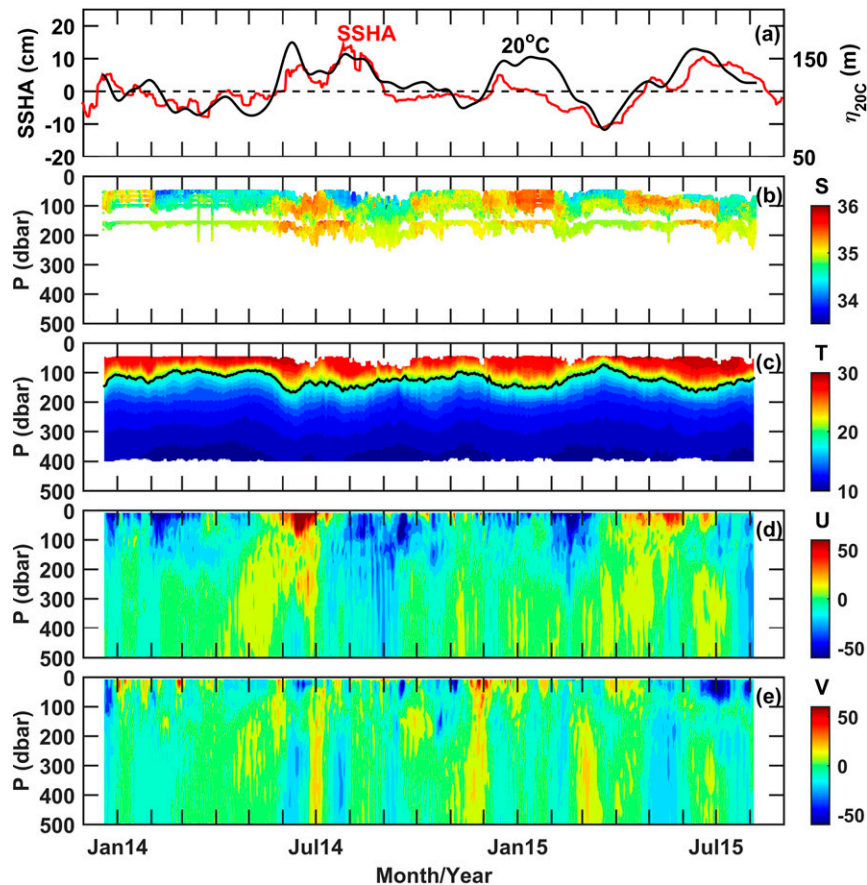


FIG. 2. Currents, temperature, and salinity observations at NRL1 (5°N , 85.5°E). (a) SSHA (red) from AVISO and 20°C isotherm depth (black) at the mooring location. (b) Scatterplots of 10-min sampled salinity (S) at five depths along the mooring line. (c) 36-h-averaged temperature (T ; $^{\circ}\text{C}$) where the black line is the 20°C isotherm, (d) zonal velocity (U), and (e) meridional velocity (V) (cm s^{-1}).

generally larger during the summer monsoon (about 10 m s^{-1}) than during the winter monsoon (about 6 m s^{-1}). Over the mooring deployment period, the average speed of the winds was 6.1 m s^{-1} . The principle ellipse at 12°N , 90°E is oriented 38.6° counterclockwise from the east, with major and minor axes of 6.5 and 1.9 m s^{-1} , respectively. Winds at the equator are weak and adjust slowly during transitions compared to the interior of the BoB (Figs. 8c–f). Wind observations were measured at a location (6.46°N , 79.98°E) at a western coastal site of Sri Lanka using a weather station with standard meteorological sensors but were not representative of the winds in the interior of the BoB due to island effects.

Several deep CTDs (not shown) were taken during the deployment and recovery of moorings in late December 2013 and early August 2015 and also during the survey cruise in June–July 2014. The CTD profiles, collected in December, during the NE monsoon near 5° – 6°N , 85° – 87°E , showed nearly uniform temperature

in the upper 70 m, but the salinity in the upper 125 m was stratified with a salinity maximum between 50 and 125 m (Wijesekera et al. 2015). The CTD profiles taken during the summer of 2014 and 2015 were similar to the winter observations but with a deeper, subsurface, high-salinity maximum between the depths of 70 and 150 m. Although the NRL moorings did not resolve the full water column salinity profiles (Figs. 2b, 3b, 4b, 5b, 6b, 7b), the time series of salinity at limited depths showed the existence of subsurface, high-salinity water in the southern BoB. The density stratification was strongest between 70 and 200 m with a buoyancy frequency of about 10–15 cycles per hour (cph). The buoyancy frequency was about 5 cph below 200 m.

4. Sea surface height variability

The time series of moored currents and hydrographic fields comprised two winter monsoon and two

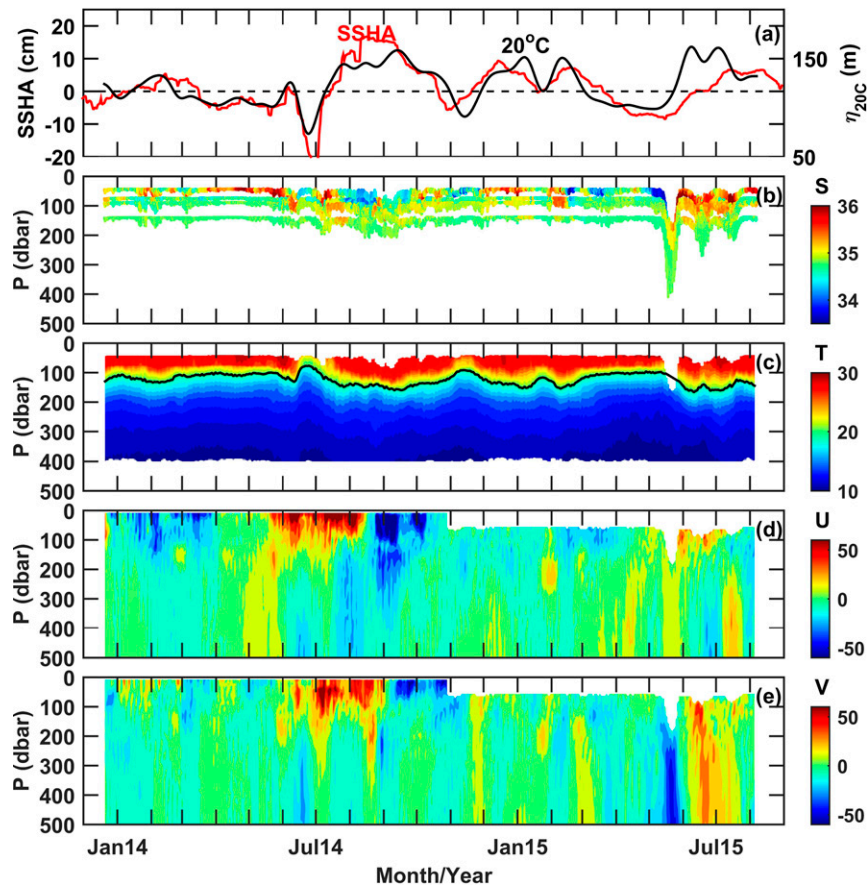


FIG. 3. As in Fig. 2, but at NRL2 (6.5°N, 85.5°E).

summer monsoon seasons between December 2013 and August 2015, during which multiple space- and time-scale low-frequency events passed through the mooring array as illustrated in the time–depth plots of currents and temperature (Figs. 2–7) and time–longitude plots of SSHA (Fig. 9). Here, we used SSHA data from AVISO with daily, 0.25°, spatially gridded products and explored both seasonal (periods larger than 120 days) and intra-seasonal variabilities (periods between 20 and 120 days). SSHA varied seasonally over the mooring array (Figs. 9a–c). However, the seasonal cycle of SSHA is most pronounced for the southern part of the array at 5°N, even though the magnitudes of SSHA were smaller than at 6.5° and at 8°N. During May–September 2014, the seasonal SSHA, as large as ± 20 cm, propagated westward at speeds of about $9\text{--}14\text{ cm s}^{-1}$. Note that the slope of the longitude–time plots of SSHA reveals the propagation speed. In July 2014, the mooring array measured a large, cyclonic eddy (Fig. 10a), and in August the array measured an anticyclonic eddy (Fig. 10b). These eddies were large enough to overlay the entire mooring array. These mesoscale features were

approximately 300 km long and 200 km wide. Therefore, an eddy, 200 km in diameter, would take 17 to 26 days to pass over a mooring with a westward speed of about $9\text{--}14\text{ cm s}^{-1}$. The cyclonic eddy, which generally forms during the summer months, is referred as the Sri Lanka dome (SLD) and is largely driven by the wind stress curl (Vinayachandran and Yamagata 1998). The positive wind stress curl over the central BoB reinforces an upwelling westward-propagating Rossby wave (e.g., McCreary et al. 1996). As the wave approaches Sri Lanka, it is amplified by strong, local, positive wind stress curl and partial reflection. The SLD forms east of Sri Lanka generally during May, matures in July, and then disappears in September (Vinayachandran and Yamagata 1998). The SLD is located just south of the positive (cyclonic) wind curl on 1 July 2014 (Fig. 10c) and northeast of the positive wind curl on 15 August 2014 (Fig. 10d). The SLD and major mesoscale features will be further discussed in section 7.

The propagation of intraseasonal oscillations is clearly visible from the 20–120-day bandpass-filtered SSHA (Figs. 9d–f). These intraseasonal oscillations propagated

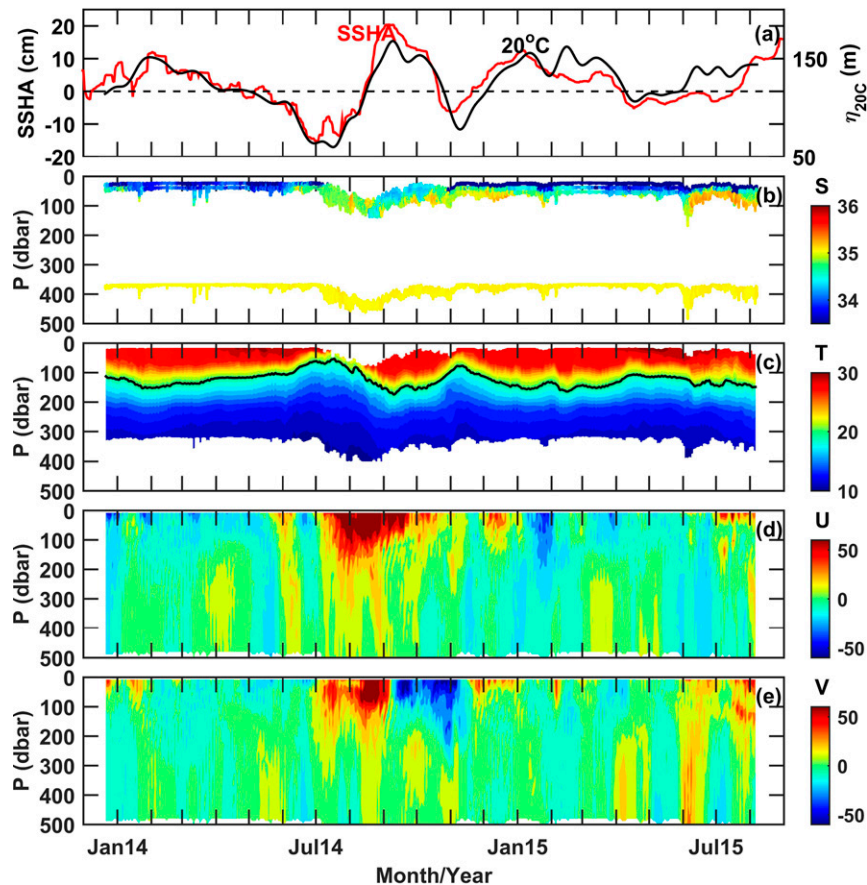


FIG. 4. As in Fig. 2, but at NRL3 (8°N, 85.5°E).

westward at a speed of about 21 cm s^{-1} , which is consistent with the propagation speed reported by Girishkumar et al. (2011) for the same latitudinal band. Note that the westward propagation of seasonal fluctuations is a factor of 2 smaller than that of intraseasonal fluctuations. The velocity structures of seasonal and subseasonal fluctuations will be discussed later in section 6.

5. Statistics of seasonal currents

Basic statistics were computed for each mooring for the winter (December 2013–April 2014 and November 2014–April 2015) and summer (June 2014–September 2014 and June–August 2015) monsoon periods (Tables 3 and 4). The hourly data were smoothed using a boxcar filter with a width of 6 h. In the following, the 6-h, averaged, east–west and north–south velocity components are represented by u and v , respectively. Statistics for the velocities at 8, 80, 160, 240, 320, 400, and 480 m are shown in the two tables. The standard error listed here is defined as the standard deviation divided by the square

root of the number of degrees of freedom, which is estimated as the sample period divided by the integral time scale. The integral time scale is defined as the discrete integral of the time-lagged autocorrelation function from zero lag to the first zero crossing after demeaning and detrending the time series.

Integral time scales during the winter monsoon for u generally ranged from about 10 to 20 days. Correspondingly, scales for v ranged from about 1 to 2 weeks. Scales often increased with depth. Integral time scales displayed similar trends for the summer monsoon except for the scales sometimes decreasing with depth. The longer time scales in the u component likely correspond to periods of stronger flow due to the SW monsoon current and an anticyclonic eddy. Integral time scales can be influenced by remote forcing in the southern BoB (Shankar et al. 2002; Yu 2003). Low-frequency SSHA, which was highly correlated with the 20°C isotherm depth (Figs. 2–7), propagated westward at a speed close to 10 cm s^{-1} (Fig. 9a). The depth of the 20°C isotherm as well as the depth-averaged currents had time lags along 6.5°N (NRL2 and NRL6) and along 8°N (NRL3, NRL4,

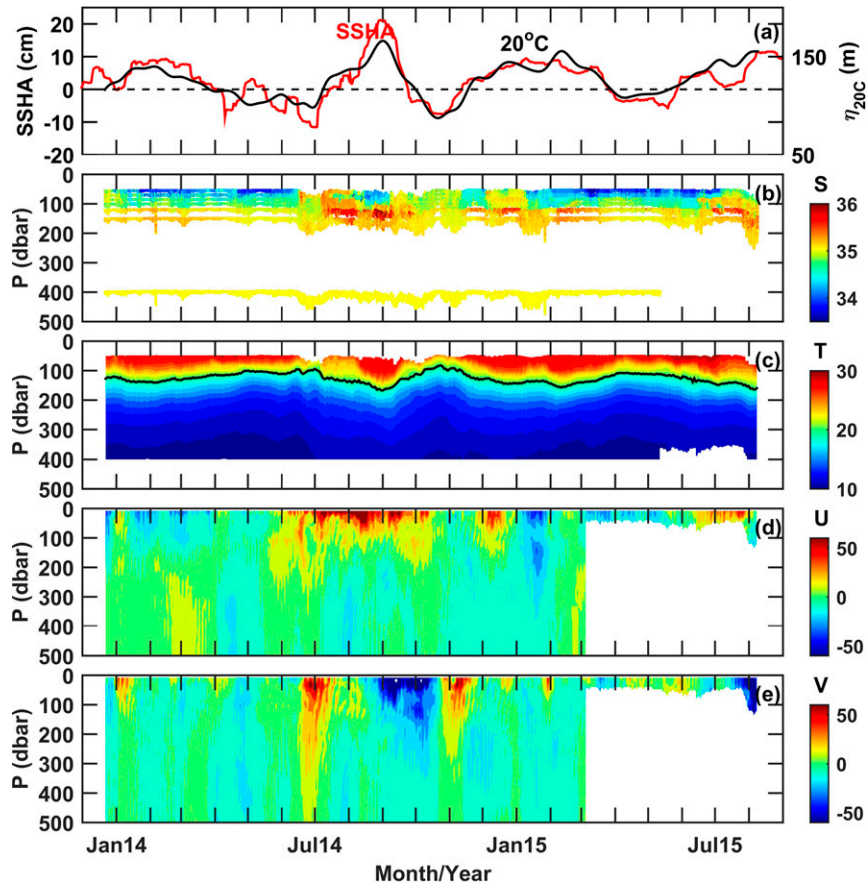


FIG. 5. As in Fig. 2, but at NRL4 (8°N , 87°E).

and NRL5; Fig. 5 in Wijesekera et al. 2016a). By matching 20°C isotherm depths between the nearest moorings and also matching vertically averaged meridional velocities, Wijesekera et al. (2016a) found 8- to 14-day time lags for 20°C isotherm features and 20-day time lags for current features at 6.5°N and 10- to 20-day time lags for the 20°C isotherm features and 25- to 30-day time lags for current features at 8°N . The integral time scales for u at the mooring locations are similar to these time lags observed between moorings. The shorter time scales in v could be related to the north-south current variability. The integral time scales for v could be indicative of the periods for the transport of salty water into the BoB.

East-west velocity components near the surface were generally larger than the north-south components but were similar at depth and much reduced in intensity. The maximum current speed observed was 198 cm s^{-1} (at NRL3 near the surface) directed toward the northeast during the SW monsoon. During the NE monsoon, the maximum current was 132 cm s^{-1} toward the southwest. Interestingly, during the NE monsoon, a period when

the winds are directed toward the south, the average v current velocity component at the surface was positive and directed northward with velocities of about 5 cm s^{-1} at all six moorings. Correspondingly, the average u current components at the surface for all six moorings were directed westward with values ranging from about 10 to 20 cm s^{-1} . During the SW monsoon, average v components were northward at the surface and at depth at NRL2 and NRL3 and were the largest observed over both monsoon periods. Correspondingly, the average u components were all westward near the surface at all the moorings but current velocities were mixed in direction at depth. Standard deviations of u and v generally greatly exceeded the mean values. Hence, the means were often not well defined.

Mean kinetic energy (MKE) and mean eddy kinetic energy (EKE) were estimated, respectively, from $(u^2 + v^2)/2$ and $[(u - \bar{u})^2 + (v - \bar{v})^2]/2$, where the overbar denotes the seasonal mean. During the SW monsoon period, EKE was higher throughout the measured levels than during the NE monsoon. Near the surface, EKE ranged from about 700 to $1600\text{ cm}^2\text{ s}^{-2}$ during the SW

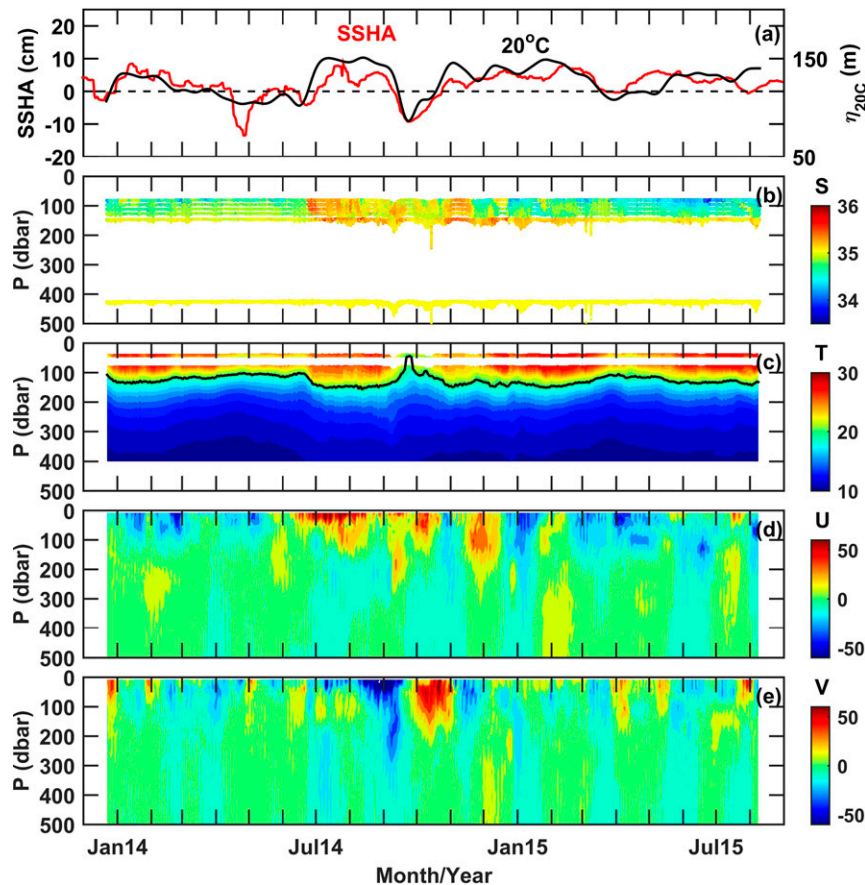


FIG. 6. As in Fig. 2, but at NRL5 (8°N , 88.5°E).

monsoon, while during the NE monsoon EKE was smaller, ranging between about 400 to $800\text{ cm}^2\text{ s}^{-2}$. Similarly, MKE was generally higher overall during the SW monsoon, with larger surface values of 950 , 1170 , and $1256\text{ cm}^2\text{ s}^{-2}$ at NRL2, NRL3, and NRL4, respectively. Both EKE and MKE rapidly decreased with depth during both monsoon periods. The inertial and tidal bands contributed less to the total energy (as discussed in section 8) and therefore the major component of MKE and EKE represent motions larger than inertial waves. The larger MKE values observed during the SW monsoon occurred during the strong eastward flows of the SW monsoon current.

Compass rose plots were computed for both the SW and NE monsoon periods. Compass rose plots provide an angle histogram of the distribution of current speed and direction along the 16 compass points (every 22.5°). The length of each bin reflects the percentage of the number of observations in that direction, and the color bar indicates the magnitude of the current speed distribution. Velocity distributions are shown for 8 and 200 m below the surface in Fig. 11. During the SW monsoon

(Fig. 11a), velocities with eastward components dominate near the surface (8 m) and are reflective of the background flow dominated by the SMC. During the NE monsoon (Fig. 11b), velocities with westward components dominate near the surface (8 m) and are reflective of the wind-driven background flow of WMC. Anticyclonic eddies and the SLD also impact the velocity distributions (Figs. 2–7). The distributions of the velocities at 200 m indicate much weaker flows where the directions are more variable and sometimes dominant directions are nearly opposite those near the surface. Near-surface velocity distributions are not representative of velocities at deeper depths.

6. Multiple time-scale variability

Currents in the interior of the southern BoB can change over time due to the effects of eddies, equatorial waves, monsoon winds, and monsoon currents, and the current patterns are not stationary. Conventional Fourier analysis assumes that the data are stationary and provides information about the average amplitude and phase for

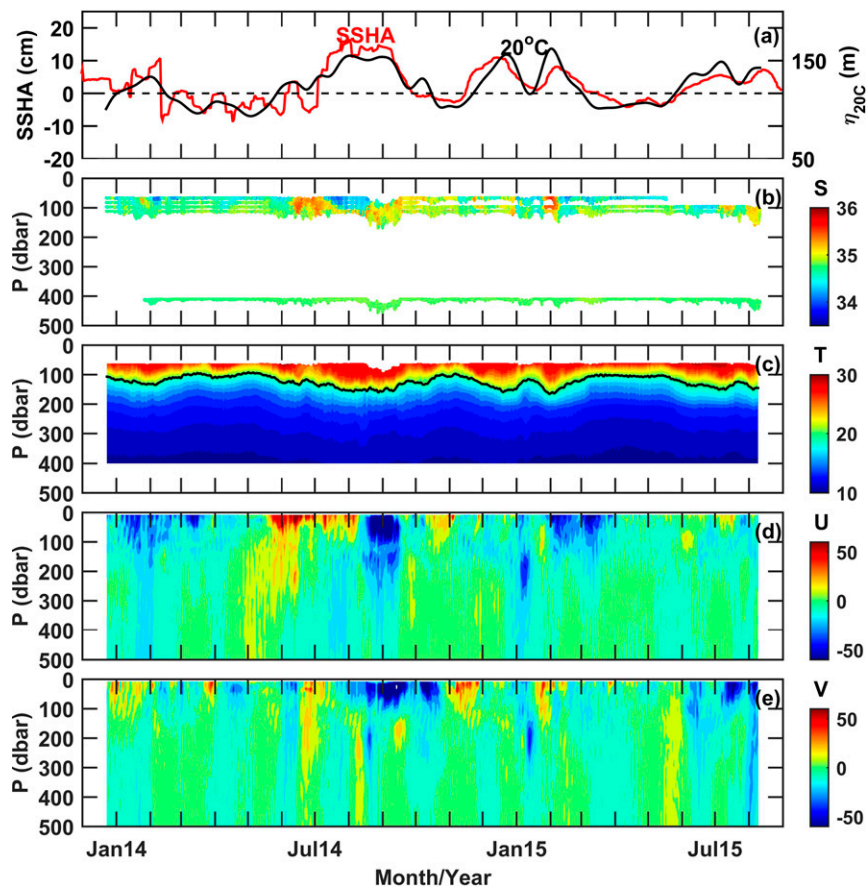


FIG. 7. As in Fig. 2, but at NRL6 (6.5°N, 87°E).

each harmonic and energy content over the entire time span of the data record. This method does not provide information on the energy levels of nonstationary processes such as near-inertial currents within specific limited time segments of the data record. Wavelet analysis of ocean currents (Liu and Miller 1996; Teague et al. 2014) provides a method for obtaining time-frequency information of nonstationary processes. The ADCP velocity time series in the BoB contain significant fluctuations in kinetic energy. Here, both wavelet and convectonal Fourier analyses are used to identify dominant motions, including event scale as well as continuous processes; to show the relative importance of the variability in the diurnal and semidiurnal tidal bands, inertial band, and lower frequency to seasonal bands; and to relate the variability to local hydrographic conditions.

Energy for the total current velocity at 120-m depth from the wavelet analysis is shown in Fig. 12a for NRL3. In general, the wavelet spectrum at this location captures the major features such as tides, inertial, and low-frequency motions found in the mooring array. Inertial and higher-frequency motions appear throughout the

year. However, a band of synoptic-scale fluctuations between near-inertial and 20-day periods shows a lower energy during March–May and higher-energy levels during June–January. The near-inertial frequency band varied with time and location. The nonstationary nature of near-inertial wave generation can be identified from the wavelet power levels in August 2014, which coincided with the passage of an anticyclonic eddy with large negative relative vorticity ($\sim 50\%$ of the local inertial frequency) over the mooring array (for vorticity, see section 8). As indicated in the wavelet spectrum, the near-inertial period of about 125 h (frequency $\sim 8 \times 10^{-3}$ cph) is significantly larger than the inertial period of 86 h (frequency $\sim 11.627 \times 10^{-3}$ cph) at 8°N. The decrease in frequency is consistent with the contribution of negative relative vorticity, where the effective frequency $f_{\text{eff}} = f + s/2$, s is the relative vorticity, and f is the inertial frequency. Bursts of energy occurred throughout the record in the near-inertial band, with the strongest inertial energies occurring during the summer monsoon of 2014. Conventional spectra of combined meridional and zonal components averaged over a depth range of 120–160 m

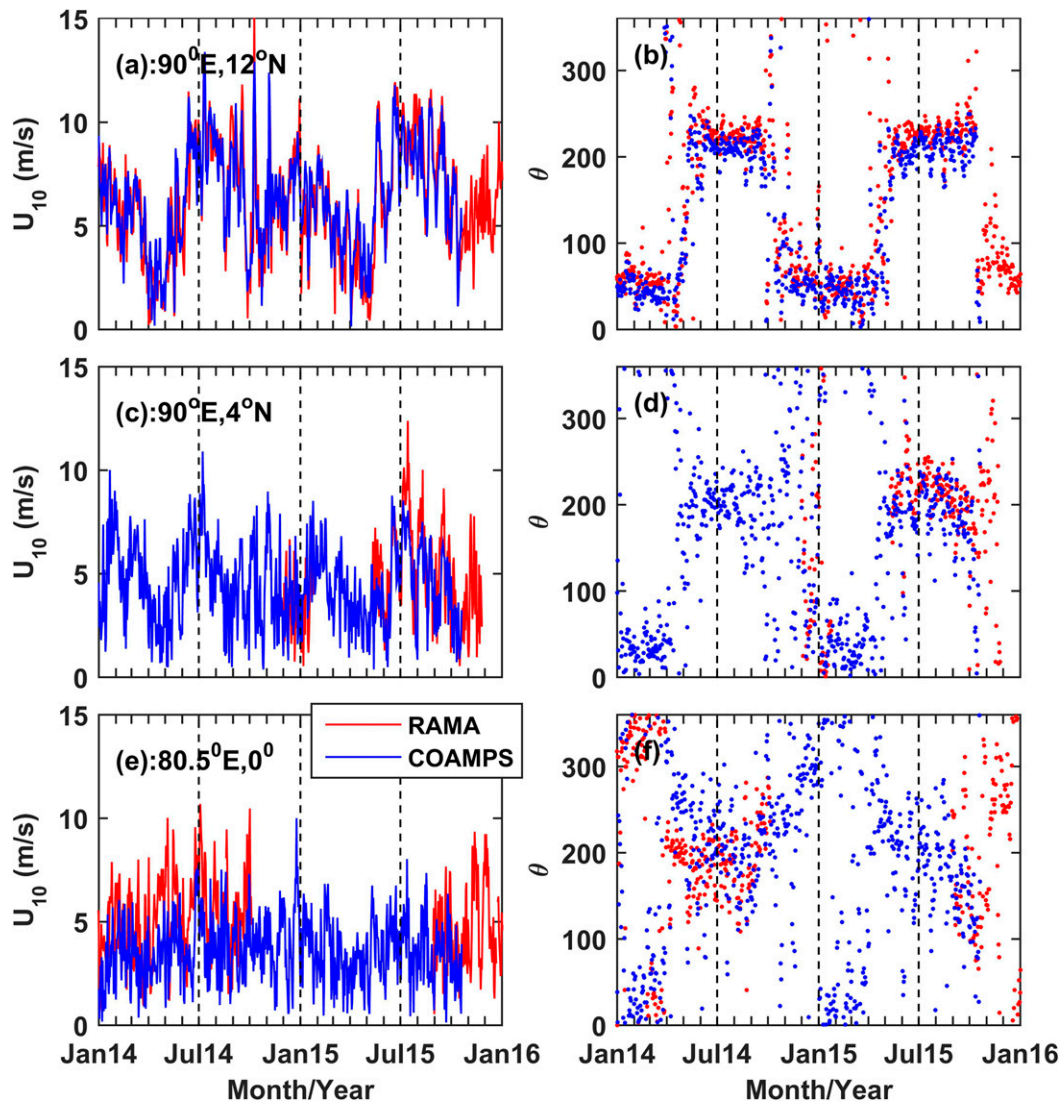


FIG. 8. Wind speed and direction from RAMA (red) buoys and COAMPS products (blue) at (a),(b) $12^{\circ}\text{N}, 90^{\circ}\text{E}$, at (c),(d) $4^{\circ}\text{N}, 90^{\circ}\text{E}$, and at (e),(f) $0^{\circ}, 80.5^{\circ}\text{E}$. RAMA winds were measured at 10 m above the sea surface. Here, oceanographic convention is used for wind direction. The direction indicated is the direction towards which the wind is blowing (http://www.pmel.noaa.gov/tao/proj_over/refresh.html).

for NRL1–6 are plotted in area-preserving form (Fig. 12b). Both analysis techniques captured the semi-diurnal tide with super harmonics, diurnal tide, and inertial bands and low-frequency motions in the southern BoB (Fig. 12). Most of the tidal energy was concentrated in the semidiurnal band; tidal energy in the diurnal band was much smaller. Harmonic tidal analysis shows that M_2 and S_2 were the dominant semidiurnal constituents, with amplitudes of about 3 and 1 cm s^{-1} , respectively; K_1 , O_1 , S_1 , and P_1 were the main diurnal constituents, with amplitudes of only about 1 cm s^{-1} .

Multiple low-frequency oscillations were found, including intraseasonal with time scales ranging from 10 to

120 days and seasonal with a time scale close to 180 days (Fig. 12). Significant energy levels were found at the lower frequencies near 20–40-, 50–70-, and 165–180-day periods. Some energy bursts, at mostly shallower levels (less than 100 m), occurred sporadically throughout the records near 10-day (200–300 h) periods. The intra-seasonal oscillations (ISO) were further examined by bandpass filtering of velocity and temperature for the 20–120-day band (Fig. 13). Temperature fluctuations as large as $\pm 3^{\circ}\text{C}$ (Figs. 13a,d) were found in the strongly stratified thermocline (Figs. 2, 4). The magnitude of temperature fluctuations became small below 200 m but extended at least up to depths of 500 m. Velocity

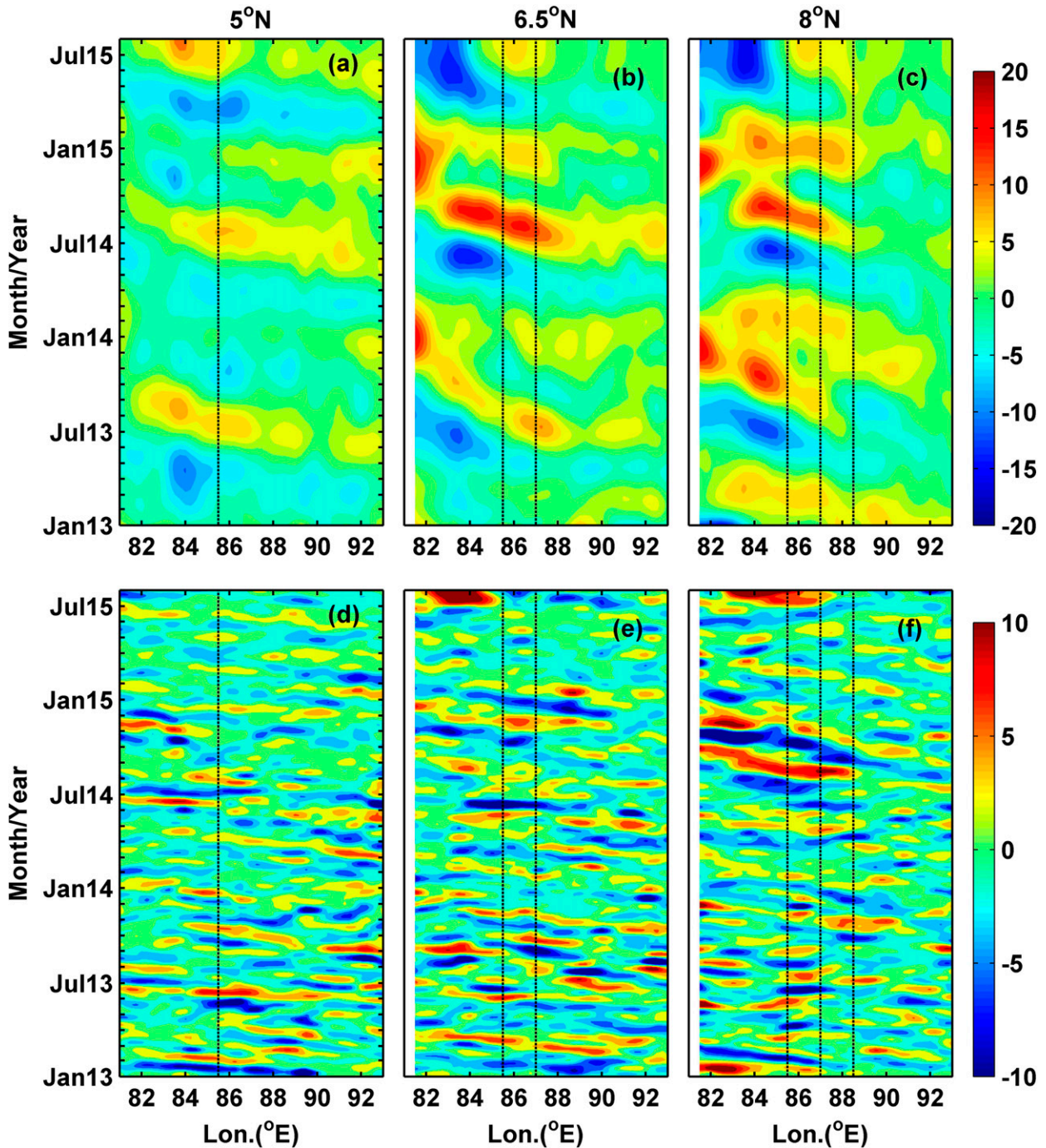


FIG. 9. Longitude–time (Hovmöller) diagrams of SSHA (cm) at (left) 5°N, (center) 6.5°N, and (right) 8°N. Thin black lines indicate the NRL mooring locations. (top) 120-day low-pass filtered SSHA and (bottom) 20–120-day bandpassed-filtered SSHA.

fluctuations were in excess of 25 cm s^{-1} (Figs. 13b,c,e,f). Although velocity fluctuations were strongest in the upper 100 m, high-energy bursts also occurred below 200 m. The largest current and temperature fluctuations in the upper 200 m at NRL3 were found during the 2014 summer monsoon, when both the SMC and mesoscale

eddies were largest (Fig. 4). Similar ISOs found in the SSHA in the 6°–8°N band (Fig. 9f) propagated westward at speeds of about 21 cm s^{-1} , close to the phase speed of intraseasonal Rossby waves, which have been reported by Girishkumar et al. (2011) at 8°N, 93°E in the southeastern BoB.

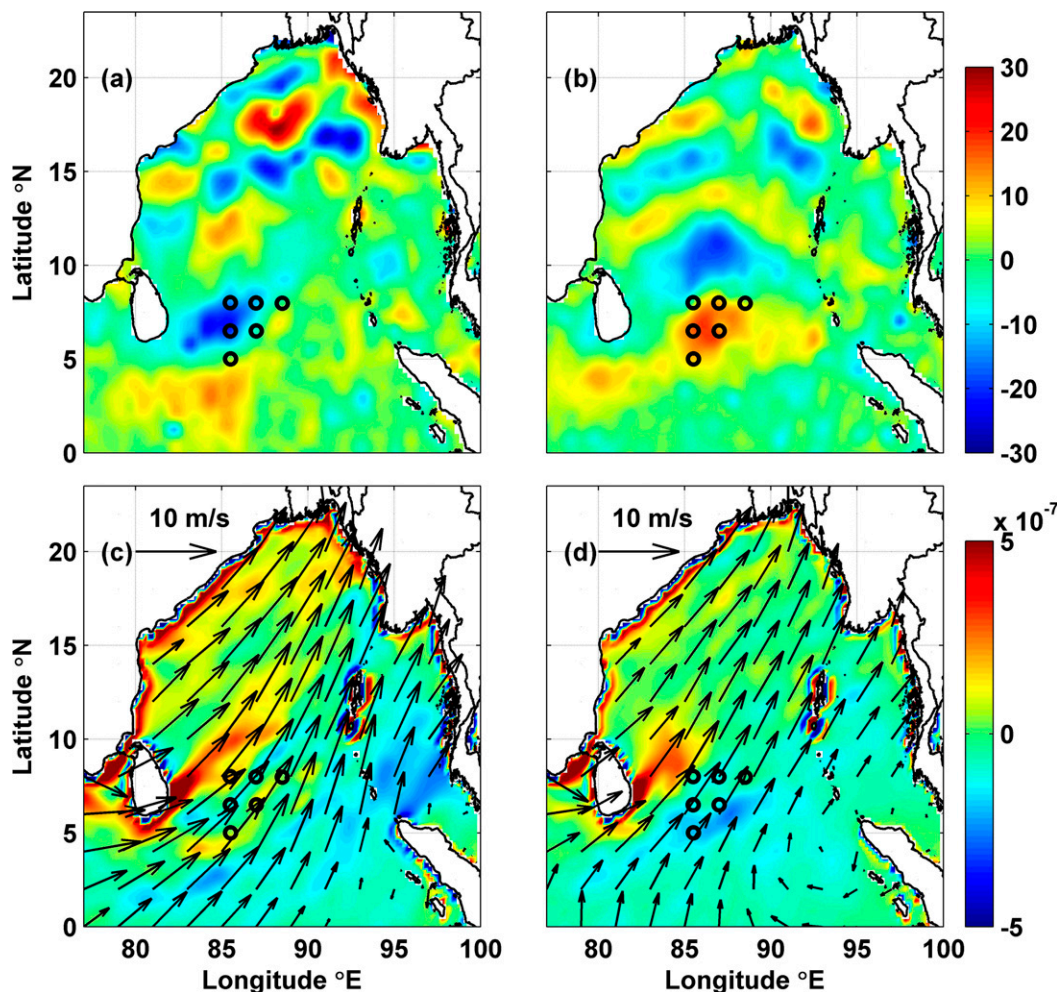


FIG. 10. SSHA (cm) maps for (a) 1 Jul 2014 and (b) 15 Aug 2014 from AVISO. Wind stress curl (color; N m^{-3}) and wind vectors (arrows; m s^{-1}) for (c) 1 Jul 2014 and (d) 15 Aug 2014 from COAMPS model results. All variables were averaged over 10 days centered at 1 Jul and 15 Aug. Black circles denote the mooring locations.

The energy ratios for currents with periods longer than 8 days to total currents were computed for selected depth levels at each mooring and averaged over the deployment periods. Currents at frequencies lower than the inertial period (3 to 6 days) accounted for 60%–80% of the total current energy. Generally, there was a subsurface maximum in the energy ratio in the upper 50 m, and energy ratios tended to increase with depth below depths of about 200 m, which are consistent with the vertical distribution ISO and seasonal currents (Figs. 2–7, 13). Energy ratios at NRL2 and NRL3 were larger than at the other moorings and sometimes exceeded 80%.

7. Description of monthly currents

Monthly averaged current profiles for the u and v velocity components are shown for each mooring in

Fig. 14. Here, the monthly averaged ADCP velocity profiles are used to display and describe temporal variability and vertical structure. These monthly averages contain both ISO and seasonal currents. The months of January through August 2014 were repeated in 2015 and were significantly different between years. The largest monthly averaged velocity components occurred during August 2014 when u exceeded 75 cm s^{-1} and v exceeded 60 cm s^{-1} in the upper 50 m of the water column at NRL3. During August 2015, both u and v were much smaller at NRL3. Component velocities were often oppositely directed among the moorings. Averaged current velocities were mostly westward in the upper 200 m during January through April 2014, but the u components were noticeably larger during January through April 2015.

Velocities are typically much larger in the upper 200 m and often reverse direction at depth. For example, in June 2014,

TABLE 3. Basic statistics over the NE Monsoon period (Nov–Apr) for selected depth levels. Columns correspond to mooring, measurement depth z , average current component \bar{U} , standard deviation σ_u , standard errors SE_u , minimum U_{\min} , maximum U_{\max} , \bar{V} , σ_v , SE_v , V_{\min} , V_{\max} , S_{\max} , D_{\max} , \bar{I}_u , \bar{I}_v , MKE, EKE

	z	\bar{U}	σ_u	SE_u	U_{\min}	U_{\max}	\bar{V}	σ_v	SE_v	V_{\min}	V_{\max}	S_{\max}	D_{\max}	\bar{I}_u	\bar{I}_v	MKE	EKE
NRL1	8	-21.38	31.06	6.40	-117.68	97.74	5.71	23.35	2.93	-92.20	111.26	132.57	241.98	21.12	7.83	244.79	754.83
NRL1	80	-6.60	13.77	2.35	-65.37	32.21	0.11	11.54	1.18	-44.09	53.51	66.64	281.19	14.49	5.18	21.80	161.42
NRL1	160	-4.90	10.05	1.91	-45.80	24.24	1.28	9.19	1.01	-35.16	40.30	49.48	229.08	17.96	6.06	12.80	92.79
NRL1	240	1.71	7.90	1.27	-62.26	26.06	1.86	8.89	1.36	-33.59	37.47	62.30	272.08	12.80	11.67	3.20	70.69
NRL1	320	4.97	6.94	1.01	-22.79	22.24	2.51	8.47	1.46	-16.39	28.57	32.36	30.57	10.51	14.81	15.50	59.92
NRL1	400	5.69	6.53	0.94	-14.32	24.85	2.95	8.15	1.41	-10.19	31.39	34.41	29.72	10.30	14.93	20.54	54.57
NRL1	480	5.12	6.12	0.99	-15.13	22.75	2.92	7.61	1.31	-18.87	25.12	28.39	27.76	12.94	14.74	17.38	47.67
NRL2	8	-18.57	20.91	6.03	-73.64	47.22	3.59	17.84	3.46	-39.20	51.27	81.73	244.28	10.97	4.97	178.85	377.61
NRL2	80	-7.89	12.39	2.14	-46.14	49.73	-0.62	11.80	1.48	-37.50	38.97	49.92	85.02	14.78	7.84	31.33	146.41
NRL2	160	-2.31	10.00	1.30	-40.77	30.10	-1.29	10.62	1.30	-32.34	31.06	43.21	250.65	8.46	7.40	3.50	106.42
NRL2	240	0.97	8.22	1.12	-31.57	32.27	-0.71	8.57	1.15	-26.41	30.44	35.78	31.72	9.27	9.00	0.72	70.50
NRL2	320	1.61	6.58	1.06	-17.02	26.36	-0.22	7.53	1.07	-22.67	23.94	28.76	141.45	12.99	10.08	1.33	50.04
NRL2	400	2.27	6.32	1.16	-14.10	24.73	0.19	7.22	1.09	-22.03	24.28	25.85	63.65	16.77	11.42	2.59	46.06
NRL2	480	2.59	6.18	1.19	-13.36	26.66	0.56	7.33	1.17	-19.54	21.56	23.96	143.34	18.43	12.76	3.51	45.94
NRL3	8	-8.79	20.68	3.56	-77.64	70.80	6.94	21.25	3.52	-106.66	70.97	112.35	161.70	14.75	13.61	62.67	439.42
NRL3	80	-4.15	12.01	1.92	-42.88	46.05	-0.92	11.01	1.42	-51.22	50.99	55.32	51.16	12.73	8.22	9.03	132.77
NRL3	160	-2.23	10.00	1.97	-35.07	32.45	-1.09	8.62	0.89	-32.84	27.67	40.71	140.91	19.33	5.23	3.09	87.14
NRL3	240	-0.01	9.04	1.90	-23.98	24.69	0.53	7.51	1.10	-22.49	23.91	30.01	55.15	21.99	10.58	0.14	69.05
NRL3	320	1.14	8.20	1.75	-23.61	22.01	1.75	7.12	1.14	-17.09	28.35	28.74	9.50	22.50	12.81	2.19	58.96
NRL3	400	1.28	7.65	1.51	-24.70	22.16	2.19	7.35	1.23	-18.49	32.22	33.19	13.92	19.39	13.77	3.21	56.29
NRL3	480	1.15	7.20	1.47	-20.10	24.44	2.18	6.92	1.16	-17.46	30.08	30.57	16.43	20.55	14.02	3.04	49.83
NRL4	8	-8.07	20.61	3.77	-60.06	64.93	7.26	18.13	2.27	-41.88	88.64	89.63	8.53	16.63	7.80	58.96	376.66
NRL4	80	-1.92	10.61	1.49	-41.26	32.80	-0.74	11.38	1.38	-28.66	54.56	54.83	5.62	8.60	6.46	2.11	121.06
NRL4	160	-1.42	9.69	1.49	-46.75	23.84	-2.32	9.17	0.99	-26.11	55.76	59.84	21.29	10.39	5.14	3.69	89.00
NRL4	240	0.70	8.23	1.49	-37.66	23.08	-2.77	7.09	0.82	-27.14	44.09	47.74	22.95	14.32	5.88	4.08	58.95
NRL4	320	0.91	8.34	1.87	-19.16	27.01	-3.10	6.51	0.83	-22.46	18.81	27.65	102.37	22.01	7.06	5.23	56.00
NRL4	400	1.18	7.83	1.83	-16.00	23.00	-2.71	5.67	0.73	-19.01	17.10	23.15	100.72	23.97	7.20	4.37	46.73
NRL4	480	1.26	7.62	1.75	-16.35	21.32	-1.71	5.62	0.73	-17.14	16.16	23.26	52.29	23.14	7.33	2.26	44.81
NRL5	8	-11.95	20.25	3.74	-73.26	56.33	4.81	18.12	2.36	-57.86	61.82	73.33	272.58	16.87	8.43	82.98	369.27
NRL5	64	-4.97	16.54	3.04	-49.18	52.40	-1.92	13.85	1.76	-44.94	50.27	56.50	127.10	16.70	8.02	14.20	232.61
NRL5	160	1.81	9.86	1.65	-31.25	34.58	0.19	8.29	0.98	-28.04	28.32	38.42	64.18	13.86	6.95	1.65	82.90
NRL5	240	4.25	7.20	1.05	-22.48	26.00	2.27	6.70	0.80	-24.89	33.58	34.08	9.84	10.55	7.13	11.61	48.35
NRL5	320	4.18	6.33	1.16	-18.60	20.62	2.48	5.93	0.86	-17.57	19.34	23.51	51.90	16.55	10.35	11.81	37.58
NRL5	400	3.57	6.12	1.18	-16.91	12.47	1.85	5.93	0.94	-16.20	20.49	25.28	62.69	18.47	12.34	8.09	36.28
NRL5	480	3.30	5.91	1.18	-16.23	12.49	1.59	5.65	0.94	-16.03	19.37	24.53	51.23	19.78	13.66	6.71	33.45
NRL6	8	-19.30	22.21	4.71	-97.27	75.82	5.21	20.66	2.43	-44.57	72.67	100.49	255.46	22.29	6.83	199.87	459.82
NRL6	80	-8.03	10.40	1.53	-40.83	27.37	-0.04	10.97	1.33	-29.69	44.61	44.64	357.75	10.75	7.26	32.26	114.29
NRL6	160	-5.51	9.55	1.16	-42.33	23.19	-1.03	8.88	0.94	-41.55	27.56	47.87	228.98	7.34	5.49	15.71	85.05
NRL6	240	-1.85	7.99	1.31	-40.08	18.79	-0.86	7.33	0.81	-42.39	24.02	46.72	205.00	13.23	6.01	2.08	58.77
NRL6	320	-0.53	6.85	1.23	-26.35	21.70	-0.39	5.97	0.82	-22.65	21.01	26.93	214.23	15.99	9.35	0.22	41.30
NRL6	400	-0.19	6.21	1.20	-24.05	19.35	-0.36	5.59	0.82	-18.33	15.20	26.01	231.30	18.39	10.77	0.08	34.86
NRL6	480	-0.33	5.90	1.17	-25.33	19.05	-0.21	5.28	0.82	-17.85	17.11	28.26	243.65	19.31	11.93	0.08	31.39

TABLE 4. Basic statistics over the SW monsoon period (June–September) for selected depth levels. Column definitions are as in Table 3.

z	\bar{U}	σ_u	SE_u	U_{min}	U_{max}	\bar{V}	σ_v	SE_v	V_{min}	V_{max}	S_{max}	D_{max}	IT_u	IT_v	MIKE	EKE	
NRL1	8	16.64	32.00	7.15	-72.15	149.75	-4.21	22.65	3.44	-76.93	76.27	161.80	67.75	21.49	9.96	147.37	768.36
NRL1	80	-12.00	23.98	5.24	-96.09	68.49	-0.34	11.61	1.42	-46.62	44.87	100.57	249.94	20.60	6.44	72.05	354.81
NRL1	160	-7.30	14.01	3.30	-44.14	39.97	0.82	10.70	1.27	-31.19	39.80	46.24	229.76	23.94	6.05	27.00	155.33
NRL1	240	-2.11	16.46	3.85	-41.83	85.76	-1.18	11.72	1.73	-43.97	31.75	87.15	100.24	23.64	9.38	2.92	203.99
NRL1	320	-1.27	13.09	2.73	-34.52	56.30	-1.14	11.20	1.79	-43.46	28.90	62.36	120.16	18.75	10.96	1.46	148.46
NRL1	400	-2.22	10.93	2.08	-33.07	53.81	-0.86	10.35	1.69	-26.40	33.71	53.85	87.92	15.68	11.51	2.83	113.24
NRL1	480	-2.58	10.21	1.83	-29.71	29.10	-1.05	9.87	1.66	-25.15	31.31	31.36	3.06	13.87	12.16	3.87	100.82
NRL2	8	37.27	48.61	15.64	-69.92	145.30	22.63	30.24	10.39	-64.28	106.23	155.13	66.17	-12.62	14.40	950.56	1638.32
NRL2	80	5.24	28.95	5.91	-94.64	57.36	14.47	18.81	3.00	-34.35	85.57	99.64	294.40	18.01	11.03	118.50	595.87
NRL2	160	-4.31	15.93	3.79	-53.11	34.71	9.13	13.08	2.03	-25.72	50.91	53.57	262.47	24.43	10.44	50.97	212.36
NRL2	240	-5.13	11.66	2.06	-37.79	25.91	4.92	13.80	1.96	-42.44	45.70	53.17	219.27	13.53	8.73	25.21	163.12
NRL2	320	-3.94	10.99	1.76	-30.84	30.43	4.20	12.98	2.01	-30.92	46.95	47.36	352.42	11.07	10.32	16.56	144.63
NRL2	400	-4.44	11.49	1.85	-28.81	33.26	3.05	13.08	2.13	-32.93	41.36	46.80	322.99	11.20	11.42	14.52	151.46
NRL2	480	-4.16	11.47	1.92	-31.28	32.13	2.27	12.97	2.08	-29.93	40.99	43.31	341.03	12.10	11.24	11.24	149.80
NRL3	8	42.97	35.73	8.20	-52.24	149.06	22.27	35.94	7.14	-85.63	152.60	198.28	48.56	22.81	17.08	1170.94	1283.69
NRL3	80	17.40	25.55	5.74	-24.13	108.86	15.28	23.04	4.40	-47.96	86.68	128.71	57.75	21.82	15.83	268.27	591.62
NRL3	160	10.70	15.08	3.05	-25.62	58.33	12.44	12.40	1.98	-26.71	54.51	60.67	66.13	17.73	11.07	134.62	190.56
NRL3	240	8.27	12.55	2.22	-28.87	37.44	9.79	9.71	1.59	-19.83	39.54	51.80	40.24	13.60	11.54	82.12	125.81
NRL3	320	6.36	11.41	1.86	-25.35	34.74	6.95	10.07	1.81	-19.57	40.23	41.52	345.67	11.48	13.91	44.39	115.81
NRL3	400	5.14	10.10	1.48	-21.61	27.85	4.87	10.18	1.84	-19.53	40.42	41.27	345.30	9.26	14.14	25.03	102.83
NRL3	480	4.08	9.12	1.19	-19.40	26.48	3.50	10.52	1.92	-22.31	37.72	39.32	341.12	7.42	14.38	14.43	96.90
NRL4	8	49.23	33.76	6.74	-25.96	172.69	-9.45	32.00	7.01	-109.53	67.17	173.13	85.92	17.28	20.80	1256.45	1081.82
NRL4	80	13.87	11.80	0.69	-29.51	58.32	-1.50	22.97	2.06	-91.15	56.02	94.24	164.22	1.47	3.50	97.34	333.08
NRL4	160	8.28	9.23	1.93	-17.13	39.12	1.75	14.23	4.06	-37.51	55.86	66.26	34.84	5.35	9.92	35.77	143.77
NRL4	240	1.76	9.24	2.32	-19.11	55.72	0.69	12.26	3.52	-41.38	45.49	59.75	68.85	7.71	10.08	1.79	117.76
NRL4	320	-1.35	6.92	2.11	-20.28	20.10	0.25	9.35	2.76	-23.63	28.51	29.80	42.42	11.29	10.60	0.94	67.69
NRL4	400	-1.52	5.80	2.00	-25.62	13.88	-0.28	7.55	2.42	-21.04	23.36	25.64	267.85	14.54	12.51	1.20	45.31
NRL4	480	-1.44	5.58	1.85	-20.46	14.73	-0.16	6.92	2.10	-20.83	23.48	25.09	22.37	13.37	11.24	1.06	39.52
NRL5	8	27.45	26.63	4.13	-37.58	121.68	-14.50	30.88	5.81	-127.71	80.10	132.16	165.10	10.44	15.40	482.04	831.11
NRL5	64	6.04	16.83	1.78	-64.43	53.03	-2.62	18.33	3.17	-71.00	63.89	72.95	193.27	4.88	13.00	21.69	309.48
NRL5	160	1.48	12.17	2.04	-40.96	43.48	1.49	11.80	2.24	-44.38	36.15	53.07	124.98	12.20	15.72	2.20	143.62
NRL5	240	-0.11	8.89	1.43	-25.57	28.88	-1.91	9.41	1.58	-36.87	26.73	41.25	146.36	11.23	12.22	1.83	83.72
NRL5	320	0.29	5.86	0.97	-15.95	18.91	-1.68	6.74	10.2	-24.71	17.96	25.13	190.51	11.93	10.00	1.46	39.92
NRL5	400	0.45	5.27	0.89	-13.44	15.12	-1.81	6.13	0.93	-21.21	15.56	22.30	198.00	12.47	10.06	1.74	32.66
NRL5	480	0.70	5.14	0.85	-14.60	16.54	-1.27	5.30	0.76	-18.52	14.06	20.32	212.85	11.91	8.89	1.05	27.23
NRL6	8	15.76	29.48	6.94	-81.42	110.73	-14.07	23.87	3.88	-110.64	60.03	122.27	221.75	24.18	11.50	223.13	719.24
NRL6	80	-6.84	23.28	6.88	-90.67	32.57	-9.90	13.93	3.72	-58.26	27.50	98.45	241.38	37.81	30.93	72.41	367.95
NRL6	160	-5.70	14.22	2.97	-47.65	36.47	-1.95	13.72	1.88	-39.78	38.40	52.41	241.29	19.03	8.17	18.13	195.23
NRL6	240	-1.63	11.16	1.92	-40.56	57.94	-2.11	11.45	1.51	-40.36	34.78	70.08	125.16	12.91	7.55	3.55	127.85
NRL6	320	-2.45	7.58	1.09	-26.92	36.11	-1.53	8.30	1.16	-26.43	23.81	38.42	109.97	9.01	8.45	4.17	63.21
NRL6	400	-2.72	6.11	0.84	-21.52	17.41	-0.90	8.05	1.16	-28.23	27.18	28.95	192.85	8.32	9.13	4.11	51.06
NRL6	480	-2.51	5.68	0.74	-16.66	16.93	-0.37	7.46	1.09	-23.89	18.23	24.43	192.08	7.41	9.33	3.23	43.93

the monthly averaged u components near the surface at NRL1, NRL2, and NRL6 exceeded 50 cm s^{-1} toward the east, but NRL2 and NRL6 clearly reversed to westward near 300-m depth with average velocities of about 10 cm s^{-1} , while NRL1 reversed to westward at about 400-m depth but with smaller average velocities of only a few centimeters per second. Average u components at NRL3, NRL4, and NRL5 were much smaller near the surface with eastward velocities between about 5 and 25 cm s^{-1} and rapidly approaching 0 cm s^{-1} below 300 m. Subsurface maximums in velocities were common.

8. Currents and eddies

Multiple dynamical features passed through the mooring array, as shown in Figs. 2–7, 9, and 10. Major features are cyclonic and anticyclonic eddies, summer and winter monsoon currents, and subseasonal variability. For example, the mooring array sampled a large cyclonic eddy (referred to as the SLD) in July 2014 and an even larger anticyclonic eddy in August of 2014 (Figs. 10a,b). The SMC just south of the SLD flows eastward between the cyclonic SLD and the large anticyclonic eddy. Vinayachandran et al. (1999) described the movement of the SMC into BoB as an intrusion, where the SMC intrusion east of Sri Lanka is forced by both Ekman pumping in the BoB and Rossby wave radiation connected with the Wyrtki jet (Wyrtki 1973) in the equatorial Indian Ocean. They further suggested that the northward movement of the SMC into the BoB is due to the Rossby wave radiation from the eastern boundary. The wind-driven SLD, westward-moving anticyclonic eddy (perhaps as result of Rossby wave radiation), and the SMC are evident during the summer of 2014 (Figs. 3, 4, 5, 10). However, for this flow scenario, the current flow of the SMC can be difficult to distinguish from the similarly eastward-directed flows of the two large eddies.

The seasonally reversing wind patterns that delineate the monsoon periods are clearly shown by the wind patterns during the mooring period (Fig. 8). The SSHA closely mirrored the depth of the 20°C isotherm, where the correlations between the 20°C isotherm and the SSHA at NRL1, NRL2, NRL3, NRL4, NRL5, and NRL6 are 0.75, 0.75, 0.84, 0.84, 0.69, and 0.82, respectively. The correlation between the SSHA and the 20°C isotherm would be even stronger during June–September 2014 when the SLD and the large anticyclonic eddy with large SSHA (~ 10 – 20 cm) passed through the mooring array. Yu (2003) suggested that the relationship between the SSHA and the 20°C isotherm is not linear in the BoB due to large variations in the contributions of salinity. Based on historical expendable

bathythermograph (XBT) measurements along 6°N between 80° and 95°E , Yu (2003) reported that the amplitude of the SSH anomaly ($\sim 3 \text{ cm}$) induced by the salinity is comparable to the amplitude induced by temperature along the 6°N latitude. Our salinity measurements are very limited, and therefore it is difficult to evaluate the relative contributions of temperature and salinity in cyclonic and anticyclonic eddies. Nevertheless the high correlations between SSHA and thermocline depth as found in the southern BoB suggest that the temperature contribution is the dominant factor here.

The 120-day low-pass filtered SSHA, the 20°C isotherm depth, and the depth-averaged currents in the upper 200 m propagated westward at a speed of about 10 cm s^{-1} (Figs. 3–7; Fig. 5 in Wijesekera et al. 2016a). Our analysis shows that oscillations of the seasonal thermocline moved westward by a factor of 2 slower than that of the intraseasonal oscillations. Phase speeds of these low-frequency motions in the 6.5° – 8°N band are close to the mode-2 baroclinic Rossby wave phase speed at 8°N (Fig. 1 in Subrahmanyam et al. 2001).

Positive SSHA (anticyclonic circulation) and negative SSHA (cyclonic circulation) were highly correlated with downward and upward movement of the thermocline, respectively. Similar movement of isotherms occurred throughout the upper 400 m (measurement window) of the water column (Figs. 2–7). Analysis of the current fields in conjunction with the SSHA maps (not shown but similar to the maps shown in Figs. 10a,b) that span the entire mooring period revealed numerous realizations of the SLD, the large anticyclonic eddy, and smaller cyclonic and anticyclonic eddies. Positive U (V) values correspond to the north (west) side of the anticyclonic eddy and negative U (V) values correspond to the south (east) side of the anticyclonic eddy. Similarly, positive U (V) values correspond to the south (east) side of the SLD and negative U (V) values correspond to the north (west) side of the SLD. Note that U and V are 36-h boxcar-averaged east–west and north–south velocity components.

The SLD is clearly evident during June–September 2014 at NRL2, NRL3, and NRL4 through the large, negative SSHA, doming cooler and saltier waters, and large current velocities in the upper 200 m (Figs. 3–5). During the passage of SLD over the mooring array, isotherms rose up rapidly, thus forming a core of cold water with temperatures typically less than 25°C . At NRL2 (Fig. 3c), the isotherms rose about 50 m within a couple of weeks, indicating an upwelling speed of about 3 – 4 m day^{-1} between 50 and 100 m. NRL3 was located on the northern side of the SLD during June 2014, and a westward velocity ($-U$) component was correspondingly observed in the upper-water column. The SLD

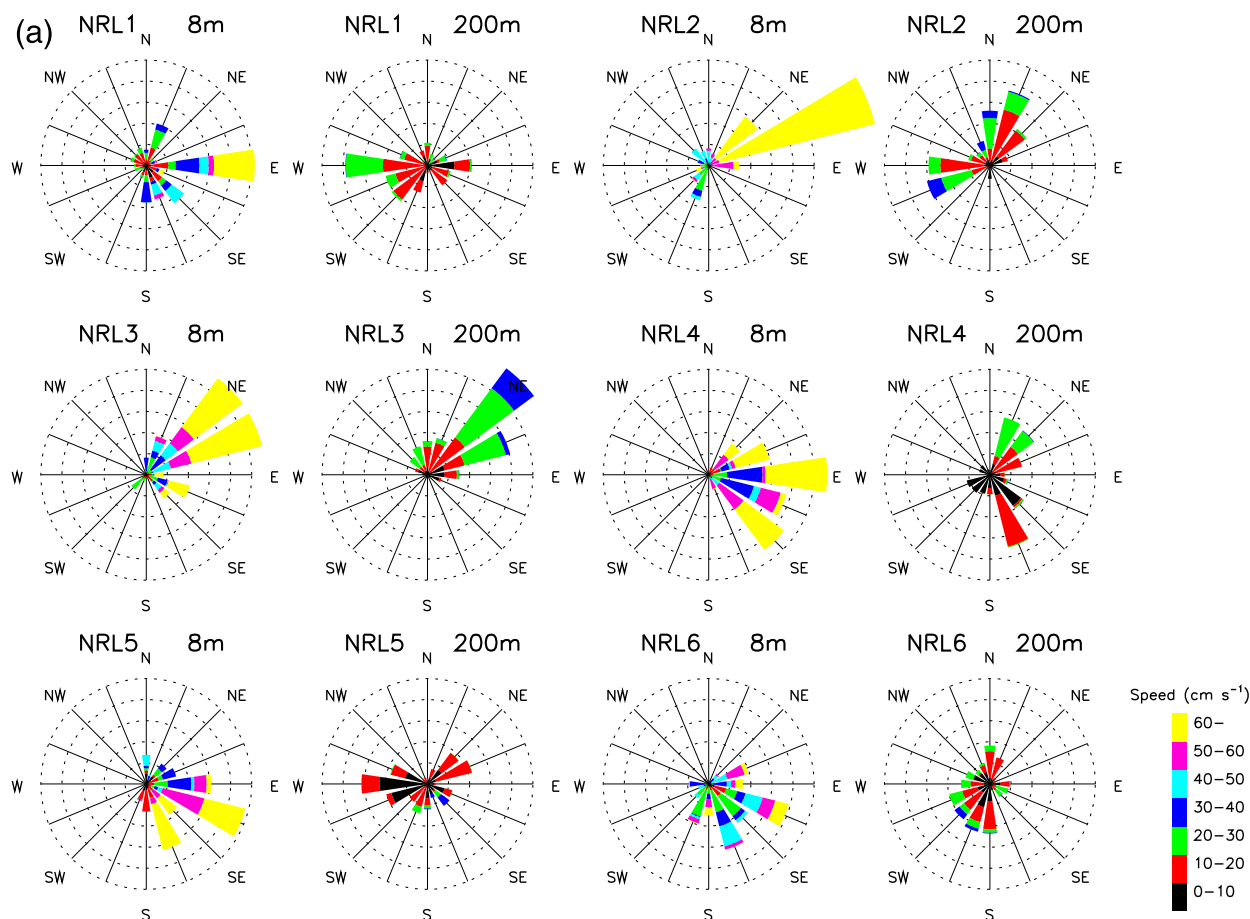


FIG. 11. (a) Compass rose diagrams for 8- and 200-m currents are shown for each ADCP mooring for the summer monsoon (May–September) period. The current directions are distributed along the 16 compass points (every 22.5°) where the length of each bin provides the percentage of the number of observations in that direction and the color indicates the magnitude of the current. Dashed rings are every 5%, with the outermost ring representing 25%. Note that the diagram shows the direction that currents are flowing toward. (b) Compass rose diagrams for 8- and 200-m currents are shown for each ADCP moorings for the winter monsoon (November–April) period.

moved northward, and the east–west velocity component at NRL3 switched to eastward ($+U$) as NRL3 was then located on the south side of the SLD. During August–September 2014, the SLD continued drifting northward, away from NRL3, and an anticyclonic eddy moved over NRL3, first with a corresponding eastward velocity component and overall northeastern flow. As the anticyclonic eddy moved toward the north and NRL3 became located over the eastern side of the eddy, the V velocity component switched to southward ($-V$) during September through October 2014, and this southeastern flow is likely due to the eddy. However, some of the eastward flow may have been due to the SMC when NRL3 was located between the SLD and the anticyclonic eddy. A large cyclonic eddy (possibly the SLD) also impinges on the moorings (NRL3, NRL4, NRL5, and NRL6) during parts of October and November 2014. The SSHA maps show that the SLD

is mostly located west of the moorings during the summer monsoon period of 2015, although there is some impingement of the SLD in July 2015. Glider surveys conducted in September 2014, along the 8°N meridian between Sri Lanka and the mooring line (NRL1–3), captured the westward-moving anticyclonic eddy and the SMC and found geostrophic velocities as large as 1 m s^{-1} carrying high-salinity Arabian Sea Water into the southern BoB (Lee et al. 2016).

COAMPS winds show a positive stress curl over the cyclonic eddy (i.e., SLD) in July 2014 (Figs. 10a,c), which is consistent with the formation of the SLD (e.g., Vinayachandran and Yamagata 1998). The strong cyclonic curl in the wind field east of Sri Lanka peaks during May–September over the SLD. Over the anticyclonic eddy in August 2014, the modeled wind stress curl was small (Figs. 10b,d). To evaluate the strength of vorticity and the associated vertical motions, the vertical

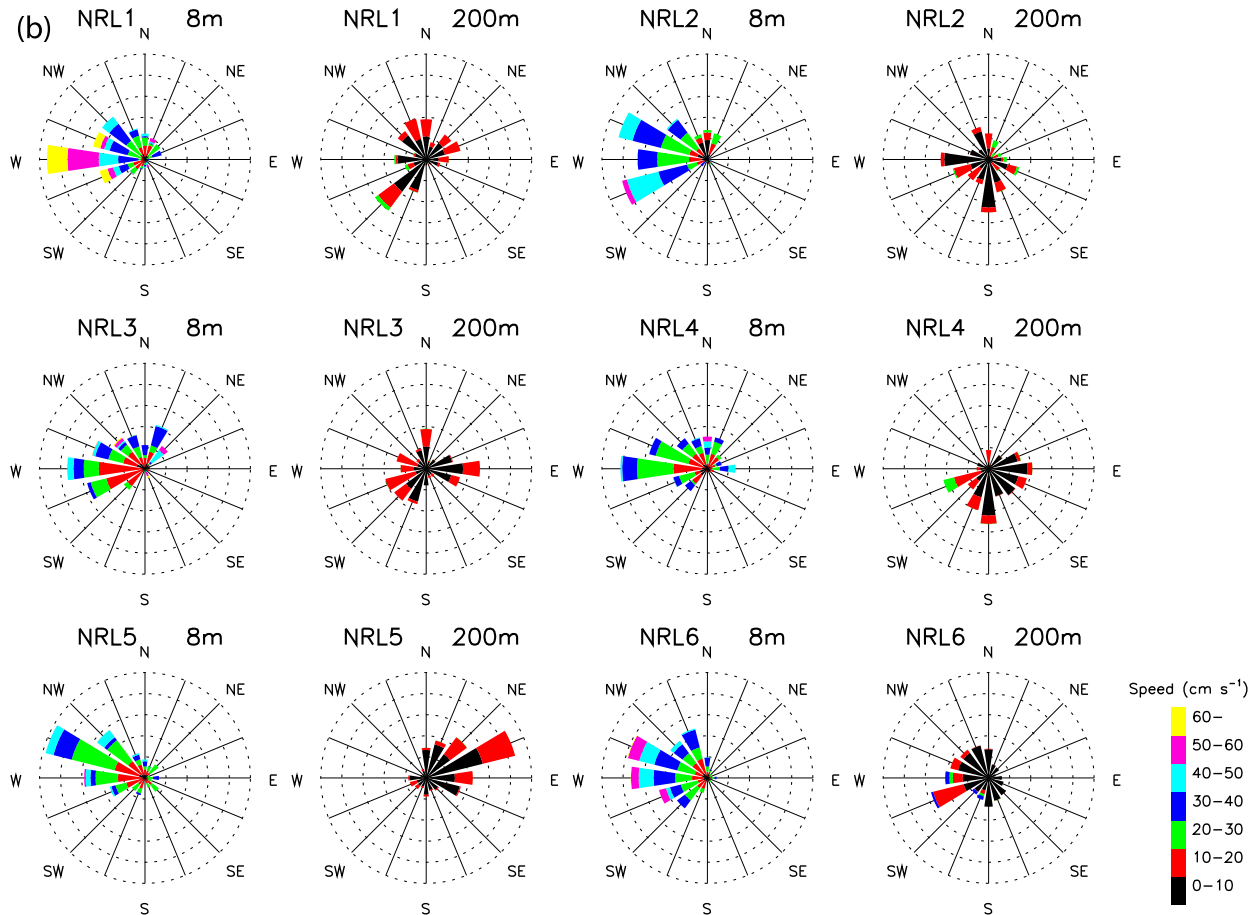


FIG. 11. (Continued)

component of relative vorticity $\zeta = \partial V/\partial x - \partial U/\partial y$ and the divergence of horizontal flow $\nabla \cdot U_H = \partial U/\partial x + \partial V/\partial y$ were computed from the velocities measured at the mooring array. Vorticity and divergences were computed for 1.5° and 3° spatial scales. Figures 15a and 15b illustrate ζ and $\nabla \cdot U_H$ for the 3° spatial scale. Time–depth structures of ζ and $\nabla \cdot U_H$ are similar for both spatial scales, but the spatial scale of 1.5° produces relatively larger ζ and $\nabla \cdot U_H$. In general, positive and negative vorticities are closely related to positive (anticyclonic) and negative (cyclonic) SSHA (Figs. 2a, 3a, 4a, 5a, 6a, 7a). Vorticity was strongest in the upper 100 m with maxima near 20–40-m depths. The cyclonic vorticity in the SLD, based on the 3° spatial scale, is about $(0.2\text{--}0.3)f_{6.5N}$, indicating that the SLD is nearly in geostrophic balance, where $f_{6.5N} = 1.65 \times 10^{-5} \text{ s}^{-1}$ is the inertial frequency at 6.5°N. However, the anticyclonic eddy passing through the mooring array during August 2014 had a vorticity of about $(0.5\text{--}0.8)f_{6.5N}$, indicating the importance of ageostrophic motions. Vertical velocity W was computed by vertically integrating $\nabla \cdot U_H$ from the

surface to a given depth with $W = 0$ at the surface. The vertical velocity at 25 m (Fig. 15c) indicates that upwelling in the SLD and downwelling in the anticyclonic eddy would be as large as 3–4 m day⁻¹. The SLD is suggested to be formed by the local wind stress curl, and therefore strong wind-driven upwelling can be expected. The Ekman pumping velocity W_E was computed from COAMPS winds and was about 1–2 m day⁻¹ over the SLD (Fig. 15d), where $W_E = \nabla \times \tau/\rho f + \beta \tau_x/\rho f^2$; $\nabla \times \tau$ is the wind stress curl, τ_x is the east–west component of wind stress, ρ is the density of seawater, f is the inertial frequency, and $\beta = 2.3 \times 10^{-11} \text{ m}^{-1} \text{ s}^{-1}$. The W_E is smaller than the vertical velocity at 25 m based on ADCP measurements, but both estimates show upwelling over the SLD. The modeled Ekman pumping was strong during summer and early fall, May–October 2014 and June–July 2015, respectively. The Ekman pumping ($W_E > 0$) over the anticyclonic eddy suggests that the local wind forcing is not related to the dynamics of this downwelling feature. Positive/negative bands of divergence and downwelling/upwelling at

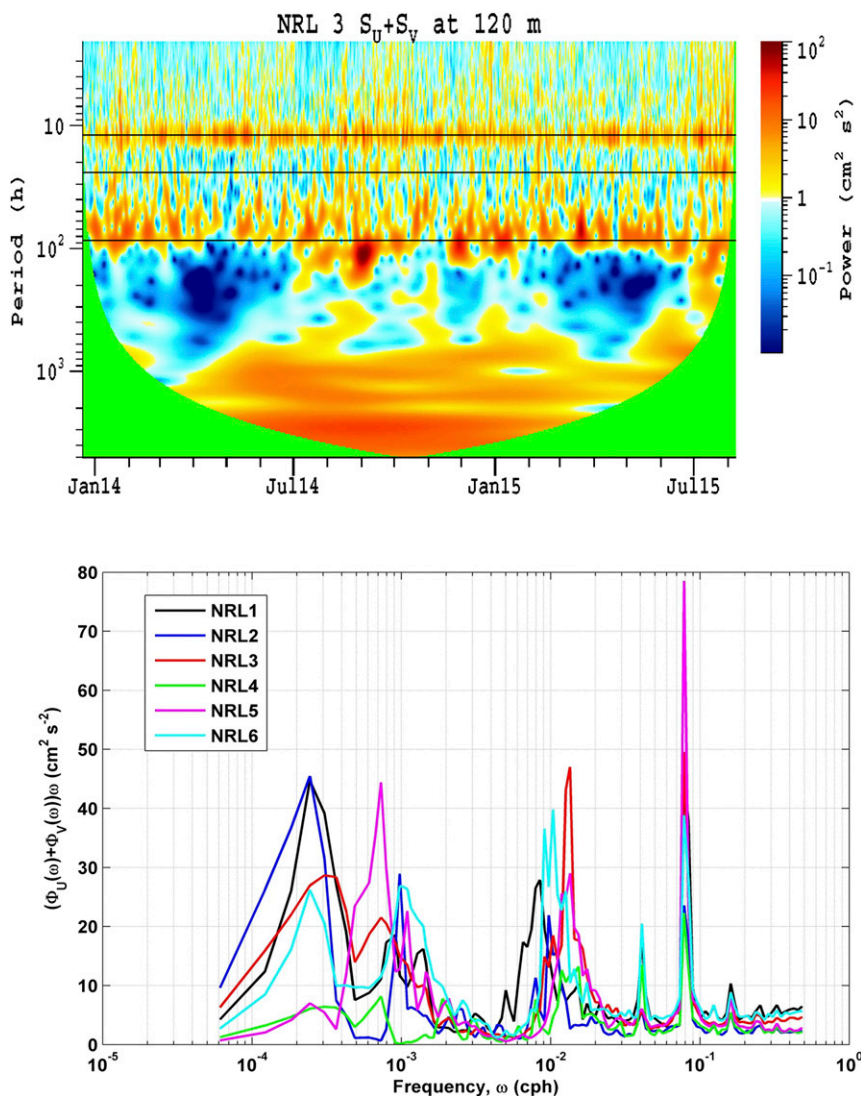


FIG. 12. (top) Wavelet spectrum of combined u and v velocity components of NRL3 at 120 m. Thin black lines represent the semidiurnal tide, diurnal tide, and inertial frequency at 8°N . (bottom) Conventional variance-preserving frequency spectra of combined u and v , averaged between 120 and 160 m for observations from NRL1–6.

30–70-day time scales (Figs. 15c,d) reflect vertical movements of the ISO.

9. Depth-averaged velocities and transports

Seasonal currents were strong in the upper 200 m, while seasonal currents were weak below 200 m but intraseasonal oscillations were significant. Therefore, the temporal variability of currents was further examined by depth averaging the zonal and meridional velocity components over two separate depth intervals (8–200 and 200–500 m). Progressive vector diagrams (PVDs) using depth-averaged velocities are plotted on a

geographical map grid for each of the moorings for upper (0 to 200 m) and lower (200 to 500 m) layers to illustrate the current flow over the measurement period (Fig. 16). The progressive vector diagram simulates the Lagrangian display of the currents from ADCP Eulerian measurements and shows how a water parcel would move if the current were the same everywhere along the track. Here, the PVDs are used to suggest where water could be transported in and out of the BoB. The PVDs originate at the mooring locations, marked by squares. The looping of the PVDs indicates some eddy variability throughout the measurement period. The PVDs indicate that the cumulative flows into the BoB are

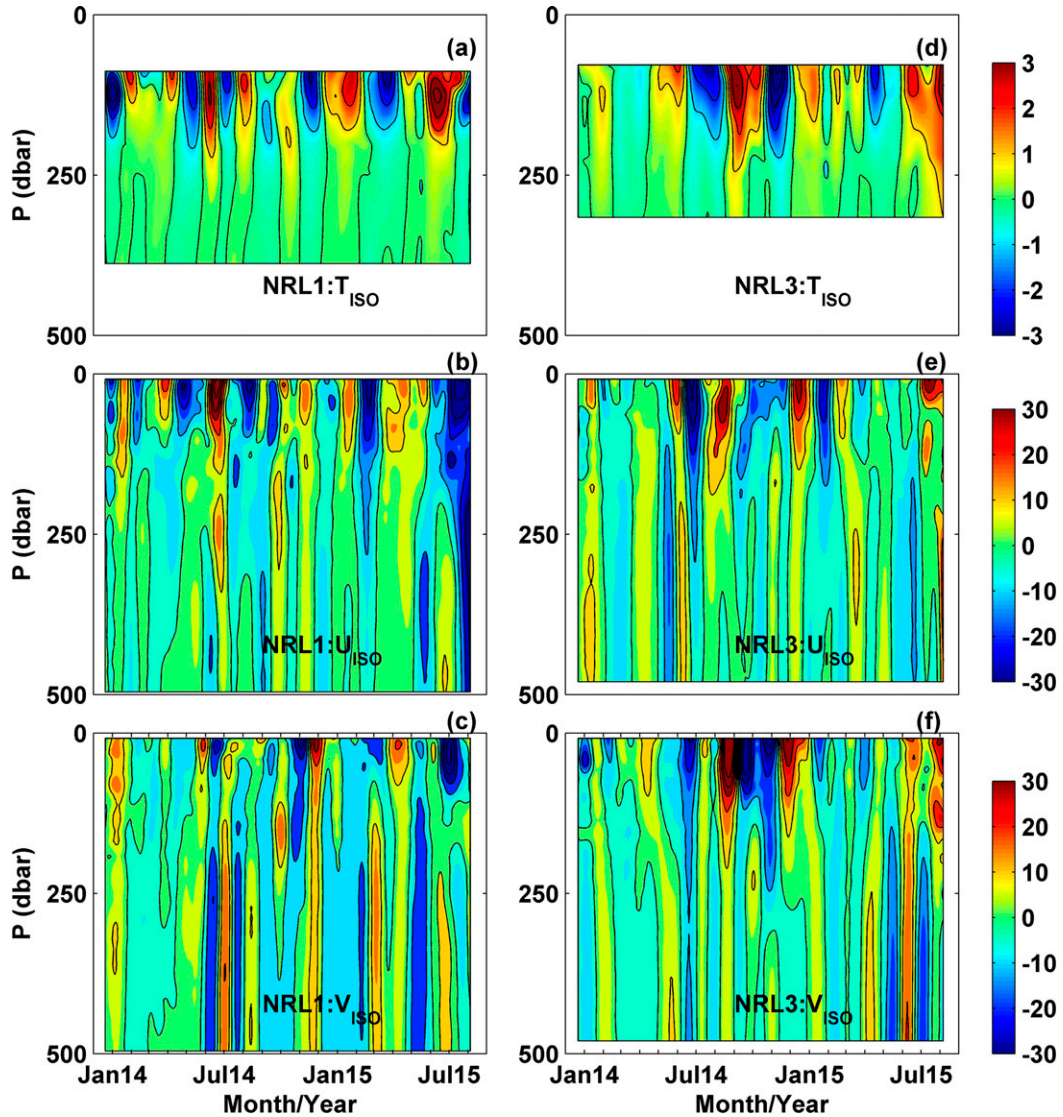


FIG. 13. ISOs representing 20–120-day fluctuations of (top) T ($^{\circ}\text{C}$), (middle) u , and (bottom) v velocity (cm s^{-1}) at (a)–(c) NRL1 and (d)–(f) NRL3.

strongest at NRL3 and are toward the northeast throughout the upper 500 m. Note that the PVD at NRL4 is short due to missing about 150 days of data at the end of the record in the lower layer. The net displacement for both layers suggests that water movement was greatest at NRL3 and was northeastward. In the upper layer, water movement was also relatively large and northward at NRL2, while movement was generally eastward at NRL4 and NRL5 and westward at NRL1 and NRL6. With the exception of the PVD at NRL3, net displacement was much smaller in the lower layer. Water movement at NRL1 was the most different between layers, being generally west-northwestward in the upper layer and northeastward

in the lower layer. Hence, surface flows are only partially indicative of the water movement in the BoB.

Depth-averaged u and v current velocity components for the upper and lower layers are shown in Fig. 17. The currents were smoothed over 7 days prior to plotting to remove inertial and shorter-period variability (the inertial period at NRL1 is 5.7 days). The averaged east-west ($\langle u \rangle$) and north-south ($\langle v \rangle$) velocities are indicative of the relative magnitude of the corresponding water movement. Current magnitudes were significantly larger in the upper layer during the summer monsoon periods, especially during 2014. The largest depth-averaged currents were observed at NRL3 during July–August 2014 and were 65 cm s^{-1} for the $\langle u \rangle$ component and 55 cm s^{-1}

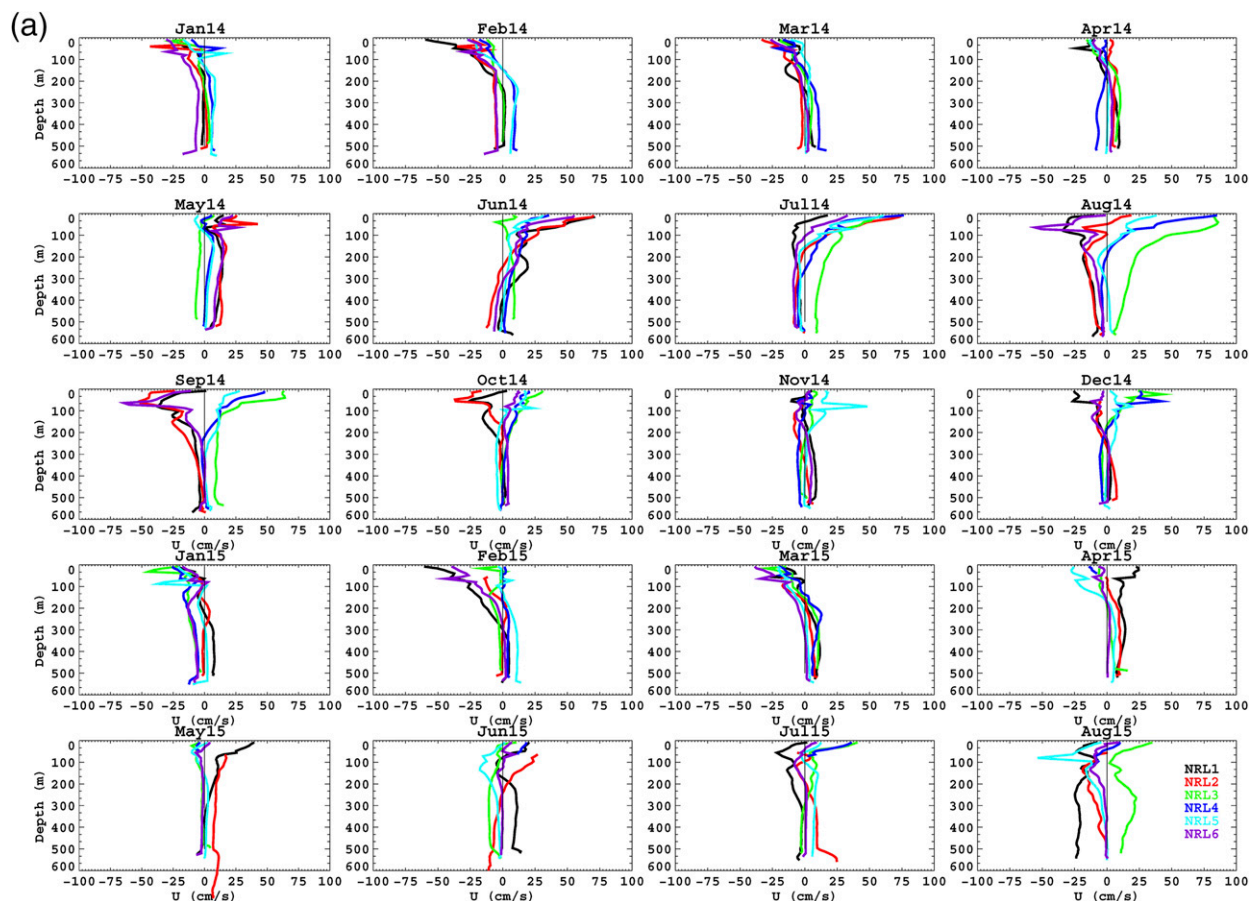


FIG. 14. (a) Monthly averaged east–west currents (u) for NRL1–6. (b) Monthly averaged north–south currents (v) for NRL1–6.

for the $\langle v \rangle$ component. Positive (negative) $\langle v \rangle$ is indicative of water movement into (out of) the BoB. Hence, the largest pulse of water into the BoB occurred during August. Both velocity components were generally less than 25 cm s^{-1} in the upper layer and 20 cm s^{-1} in the lower layer outside of the monsoon periods. The larger eastward velocity components are associated with the southern portion of the SLD eddy, the northern portion of the large anticyclonic eddy, and the SMC. The larger westward velocities were associated with the southern portion of the large anticyclonic eddy and the NMC.

During the mooring recovery cruise in August 2015, current vectors calculated along the R/V *Roger Revelle* tracks using the shipboard ADCP indicated broad currents that were 100 to 200 km in width within the region of the moorings (Wijesekera et al. 2016b). Using moored and shipboard ADCP observations south of Sri Lanka, volume transports of 10 to 12 Sv were estimated for the NMC using observations reported on by Wijesekera et al. (2016b) and transports of 8 Sv for the SMC were estimated by Schott et al. (1994) for similar width currents. Modeled transports (Shankar et al. 2002) for south

of Sri Lanka and for 85°E were estimated to range from 8 to 15 Sv.

With the large geographical separation in mooring positions, short-term and eddy current variability in the velocity data make it difficult to identify long-term trends in the transport. Cumulative volume transport (CVT) was used to minimize the short-term current fluctuations relative to the long-term mean flows. CVTs per unit width versus time were computed at each of the moorings; the depth-averaged velocity components ($\langle u \rangle$, $\langle v \rangle$) were integrated over time and multiplied by the thicknesses of the upper and lower layers (0 to 200 m and 200 to 500 m, respectively). Plots of the CVT series are shown in Fig. 18. Positive (negative) slopes in CVT for $\langle v \rangle$ are due to longer-term trends in the transport of water into (out of) the BoB. Positive (negative) slopes in CVT for $\langle u \rangle$ are due to longer term trends in the transport of water eastward (westward). Net transports per unit width are the CVT values at the end of the measurement period.

In the upper layer, CVT(u) was westward (Fig. 18a) at all of the moorings at the beginning of the measurement

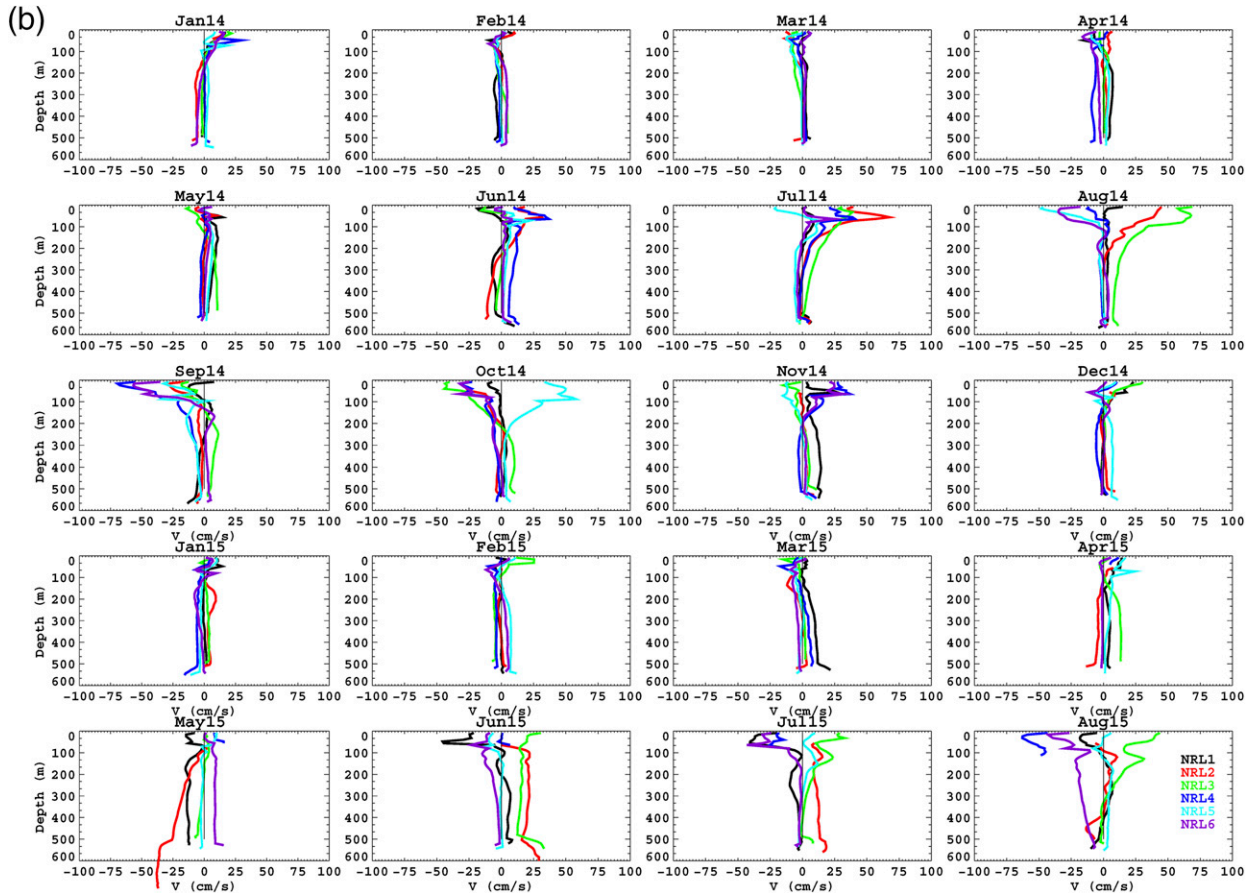


FIG. 14. (Continued)

period during the northwest monsoon prior to the onset of the southwest monsoon. Then the $CVT(u)$ switched to eastward at all of the moorings. $CVT(u)$ remained eastward until December 2014 at NRL3, NRL4, and NRL5 but only until about September 2014 at NRL1, NRL2, and NRL6, before switching westward (northwest monsoon). The SLD and an anticyclonic eddy likely affected the currents at NRL3, 4, and 5. Generally, similar but less pronounced tendencies were observed for the southwest monsoon in 2015 at the end of the measurement period.

$CVT(u)$ over the measurement period in the upper layer was eastward at NRL3, NRL4, and NRL5 with magnitudes of about 50×10^7 , 47×10^7 , and $12 \times 10^7 \text{ m}^3$, respectively. The average volume transport over the measurement period of approximately 600 days ($51.84 \times 10^6 \text{ s}$) can be estimated by dividing CVT by the measurement period and then multiplying by the width of the current. Average eastward volume transports at NRL3, NRL4, and NRL5 for a typical current width of 100 km are then about 1, 0.9, and 0.2 Sv, respectively. Correspondingly, $CVT(u)$ was westward at NRL1,

NRL2, and NRL6 with magnitudes of about 50×10^7 , 10×10^7 , and $50 \times 10^7 \text{ m}^3$, respectively. Average volume transports in the upper layer are then about 1, 0.2, and 1 Sv, respectively. Hence, the average eastward and westward volume transports were both about 1 Sv.

In the lower layer, $CVT(u)$ over the measurement period is eastward at all moorings except for at NRL6, and the record was short at NRL4. However, $CVT(u)$ frequently switched direction throughout the record on time scales of about 30 to 100 days. $CVT(u)$ at NRL1, NRL2, NRL3, and NRL5 were 35×10^7 , 10×10^7 , 35×10^7 , and $32 \times 10^7 \text{ m}^3$, respectively. $CVT(u)$ was about $9 \times 10^7 \text{ m}^3$ and westward at NRL6. The corresponding average eastward volume transports for NRL1, NRL2, NRL3, and NRL5 are about 0.7, 0.2, 0.7, and 0.5 Sv, respectively, and the average westward volume transport at NRL6 is about 0.2 Sv. The total average eastward volume transport in the lower layer across the north–south mooring line (NRL1–3) is then about 1.6 Sv and is larger than the westward volume transport at NRL6. Total average eastward transport in the upper 500 m across the north–south mooring line (NRL1–3) is then about 2.6 Sv.

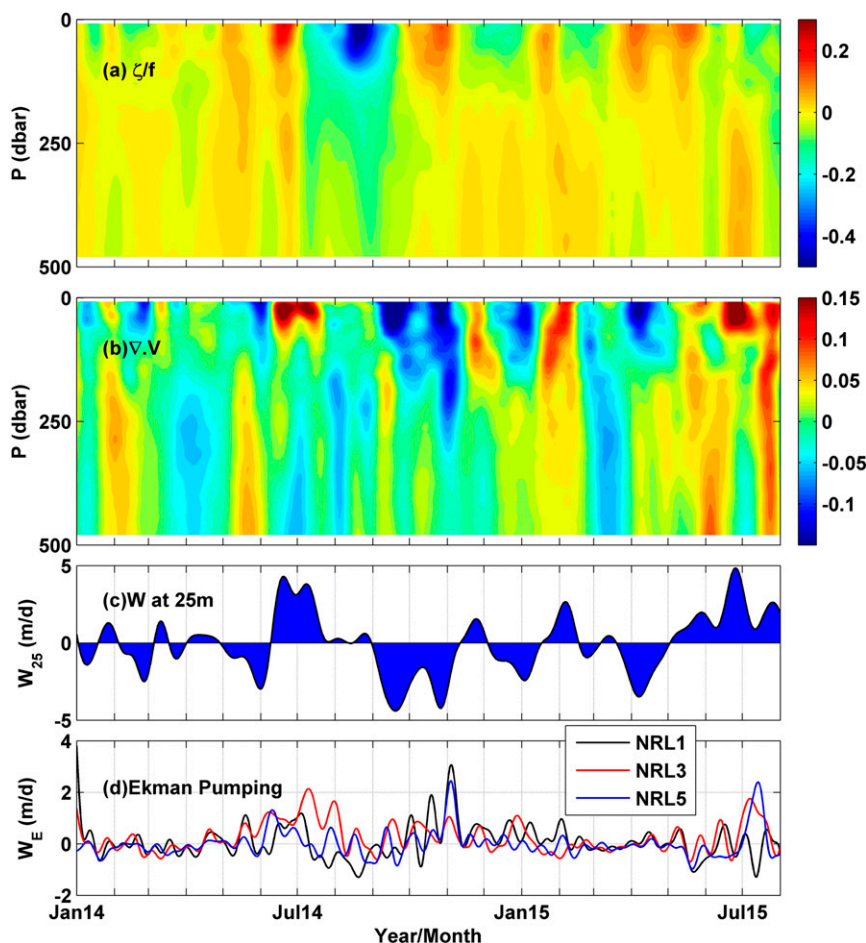


FIG. 15. (a). Normalized vertical component of relative vorticity by inertial frequency at 6.5°N , based on 20-day low-pass filtered ADCP velocities from NRL1, NRL3, and NRL5. (b) Horizontal divergence (day^{-1}) based on 20-day low-pass filtered U and V velocities from NRL1, NRL3, and NRL5. (c) Vertical velocity estimated from horizontal divergence and (d) Ekman pumping velocity based on COAMPS wind products.

Perhaps most interesting in the upper layer is the north–south CVT(v) (Fig. 18b). CVT(v) was very small until July 2014, during the southwest monsoon. Then the CVT(v) exhibited northward transport at all of the moorings and was most extreme at NRL2 and NRL3. Then the CVT switched toward the south at all the moorings in September 2014 at the end of the southwest monsoon. CVT(v) remained small from December 2014 until May 2015 and then a similar pattern emerged for the southwest monsoon during 2015. The rapid increase in northward transport was likely associated with currents from the SLD, anticyclonic eddy, and SMC. The large pulses in CVT toward the north occurred over just a few months during the southwest monsoon periods.

At NRL3, net CVT(v) (value at the end of the measurement period) into the BoB in the upper layer was approximately $43 \times 10^7 \text{ m}^3$. Therefore, the northward

volume transport for the upper layer is about $8 \text{ m}^3 \text{ s}^{-1}$. If this transport were typical for a realistic current that is 100 km wide in the BoB, then the average transport into the BoB over the 600 days is about 0.8 Sv. However, a northward CVT of about $35 \times 10^7 \text{ m}^3$ occurred over a time period of about 50 days during the 2014 summer monsoon and the corresponding average volume transport for this period is 8 Sv for a current 100 km in width. For currents 200 km in width, the transports would double, and would be 1.6 and 16 Sv, respectively, at NRL3. Hence, the northward volume transport in the upper layer occurred in pulses and was small or negligible outside of the relatively short pulse periods. CVT(u) was similar in order of magnitude but was more gradual in buildup.

Net CVT(v) in the lower layer was also greatest at NRL3 and had a magnitude of about $57 \times 10^7 \text{ m}^3$, which

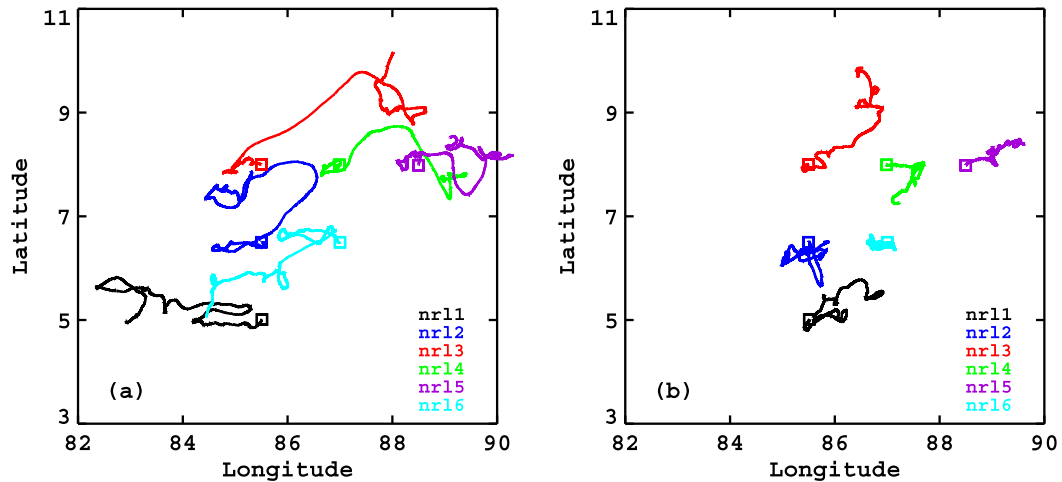


FIG. 16. PVDs for all moorings. Lines represent PVDs for depth-averaged velocities for the depths of (a) 0–200 m and for (b) 200–504 m.

was greater than the net $CVT(v)$ in the upper layer. Similarly, this net CVT would correspond to an average northward transport of about 1.1 Sv over the measurement period. However, the CVT increase in the lower layer at NRL3 was much more gradual than the pulse-like increases in the upper layer. The combined, net-averaged, northward transport from both layers over the measurement period was about 1.9 Sv at NRL3.

In the upper layer, net northward $CVT(v)$ also occurred at NRL2 and NRL5 with values of about 30×10^7 and 11×10^7 m³ and corresponding volume transports of about 0.6 and 0.2 Sv, respectively. Net $CVT(v)$ was near 0 at NRL1. Net southward $CVT(v)$ at NRL4 and NRL6 with values of 16×10^7 and 29×10^7 m³ occurred in the upper layer and corresponded to average volume transports of about 0.3 and 0.6 Sv, respectively. In the lower layer, net northward $CVT(v)$ occurred at NRL1 and NRL5, each with values of about 12×10^7 m³ and corresponding average volume transports of about 0.2 Sv. $CVT(v)$ was southward (negative) in the lower layer at NRL4 through day 800 (short record). Small $CVT(v)$ was observed at NRL2 and NRL6 except for a southward pulse at NRL2 during May–June 2015. The average northward volume transport for the upper 500 m for NRL5 is about 0.4 Sv. Southward average volume transport of about 0.3 Sv was observed for the upper layer at NRL4, but corresponding transport for the lower layer could not be calculated. Therefore, average northward volume transport for the east–west mooring line (NRL3, NRL4, and NRL5) is approximately 2.3 Sv.

Note that the estimated average volume transports assumed horizontal currents with a nominal width of 100 km. In addition, the transports are averaged over the

entire mooring deployment period of about 600 days. Instantaneous transports can be much larger. The variability of $CTV(u)$ and $CTV(v)$ in each layer clearly indicates the horizontal inhomogeneity of the current over 100–1000-km scales and can impact the hydrologic balances of the BOB.

10. Discussion

The circulation in the BoB has a dramatic seasonal variation in response to the monsoon winds. The basinwide circulation is cyclonic at the onset of the northeast monsoon and anticyclonic during the onset of the southwest monsoon (Cheng et al. 2013; Somayajulu et al. 2003; Eigenheer and Quadfasel 2000; Shetye et al. 1993). The monsoon currents in the southern BoB are eastward during the summer (SMC) and westward during the winter (WMC). During summer, the SMC interacts with a Rossby wave propagating across the BoB from the western boundary (Schott et al. 1994; Vinayachandran et al. 1999). The East India Coastal Current flows northward off the coast of India and southward off the coast of Sri Lanka during summer, southward along both coasts during winter (Mukherjee et al. 2014; McCreary et al. 1996; Shankar et al. 1996). Hydrographic observations have described the seasonal variability well in the western BoB (Vinayachandran and Yamagata 1998). The circulation patterns in the interior of the bay are affected by numerous cyclonic and anticyclonic eddies. During the 2002 fall and 2003 spring intermonsoon seasons, nine cold-core eddies were identified by Kumar et al. (2007) in the western and central BoB using satellite and hydrographic data. From satellite altimetry data, Cheng et al. (2013) found two

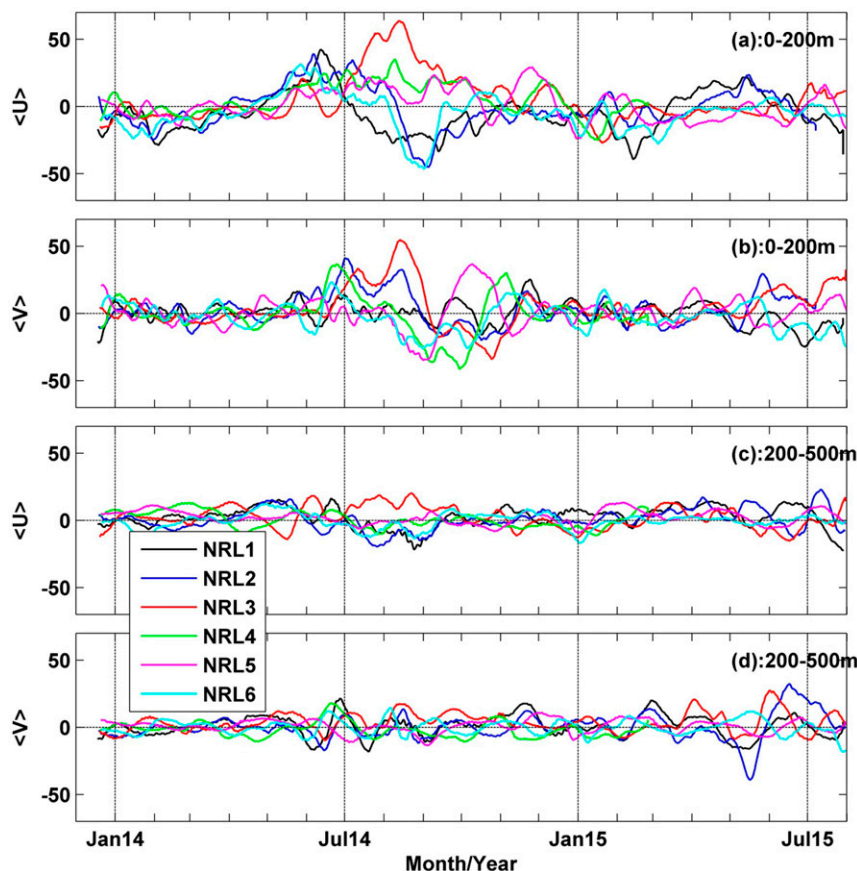


FIG. 17. Depth-averaged currents in the upper 200-m layer (a) $\langle u \rangle$ and (b) $\langle v \rangle$ for all six moorings, and depth-averaged currents in the 200–500-m layer (c) $\langle u \rangle$ and (d) $\langle v \rangle$.

distinct bands of eddy activity consisting of both cyclonic and anticyclonic eddies in the western and central BoB. The circulation is further complicated by Kelvin and Rossby wave radiation (Potemra et al. 1991; Rao et al. 2010; Suresh et al. 2013).

The westward-moving baroclinic Rossby waves likely produce the ISO signal found in SSHA, thermocline temperature, and velocities in the water column. The dominant periods of ISO were 20–40 and 50–70 days. Girishkumar et al. (2011) suggested that the remote equatorial winds could force the ISO in the thermocline in the southern BoB. The subseasonal (periods ~30–60 days) westerly wind fluctuations at the equator can generate Rossby waves with multiple time scales (30–90 days) as a result of the equatorial Kelvin wave reflections from the Sumatra coast (Han 2005; Vialard et al. 2009; Iskandar and McPhaden 2011).

There are few, if any, measurements that describe the subsurface structure of the monsoon currents and eddies east of Sri Lanka in the south-central BoB and hence the currents have been a mystery. Therefore, six moorings were deployed in the south-central BoB in international

waters, approximately 200 nm east of Sri Lanka. The major current features impacting the moorings were the SLD, WMC, SMC, and a large anticyclonic eddy. The mean current flows in the upper layer were steered by the southwest and northeast monsoons and were eastward (SMC) and westward (WMC) flowing, respectively. A large cyclonic eddy, the SLD develops during the southwest monsoon in response to the local cyclonic wind curl (Vinayachandran and Yamagata 1998) and decays at the end of this monsoon period. A large anticyclonic eddy is commonly found east-southeast of the SLD. From the NRL mooring observations during June and July 2014, the SLD is clearly indicated at NRL3 by the low in SSHA (Figs. 4a, 10a), doming of the isotherms in the upper layer (Fig. 4c) and higher salinity (Fig. 4b), large northeastward currents (Figs. 4d,e), and positive vorticity and upwelling in the cold dome (Fig. 15) along with positive wind stress curl (Fig. 10c) and Ekman pumping (Fig. 15d). Similar but less pronounced signatures are also found at NRL2 and NRL4.

From analyses of SSHA data coincident with the mooring period (e.g., Figs. 10a,b), the SLD and

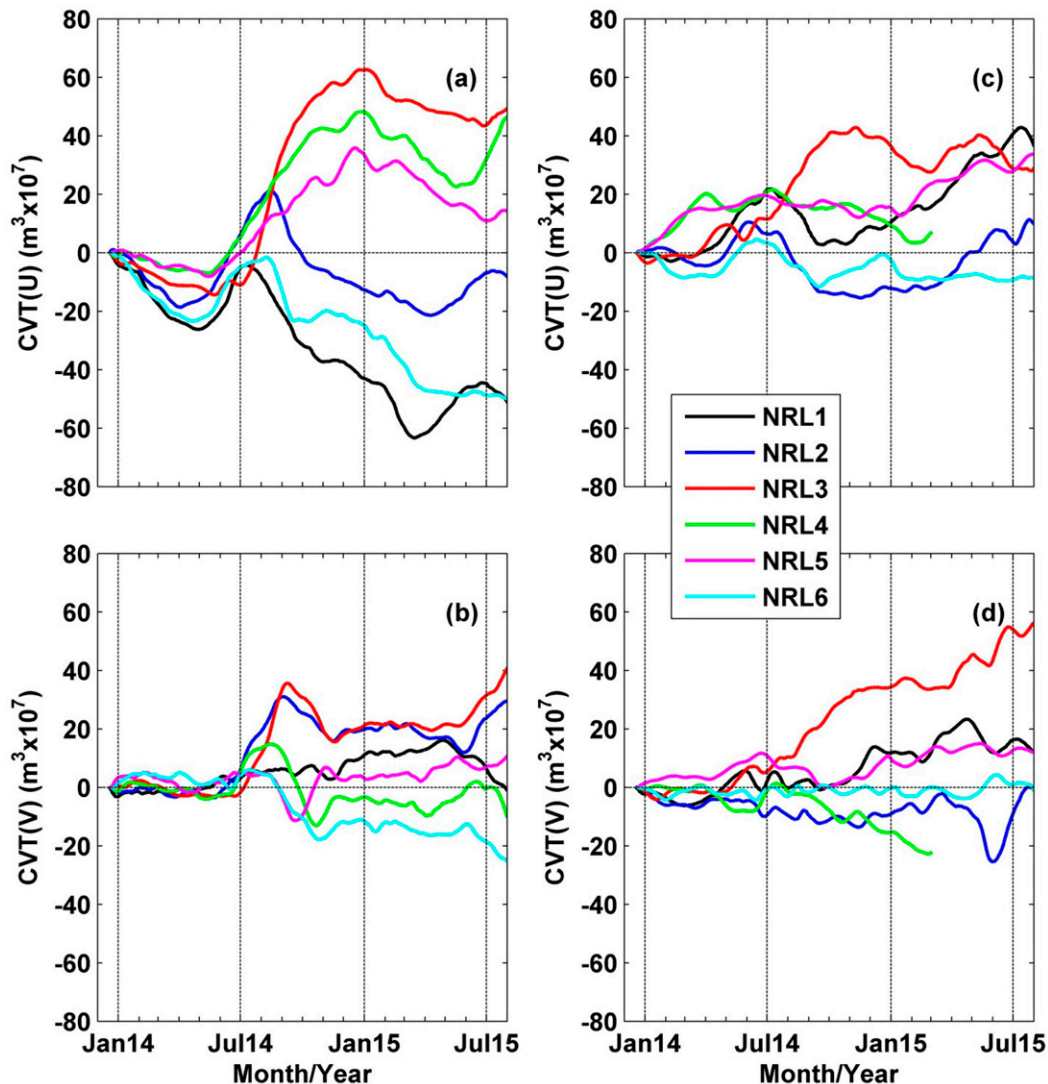


FIG. 18. CVT in the upper 200-m layer for (a) u velocity and (b) v velocity for all six moorings. CVTs in the 200–500-m layer for (c) u velocity and (d) v velocity.

anticyclonic eddy are commonly present during summer and can coexist. They are often located so that they can impact the generally eastward flow of the SMC and can steer current flow northward into the southern BoB. The positioning of these two eddies can play a significant role in pumping warmer higher-salinity water into the BoB. Northward average current transports estimated from the mooring current observations are about 2 Sv over the 20-month period and were approximately equally split between the lower and upper layers. However, much of the northward transport in the upper layer occurred in pulses that were likely related to the SLD and anticyclonic eddy. In the lower layer, transport into the BoB seemed to occur more uniformly, spread over the entire observation period. The net volume transports for

moving water into the BoB were positive at NRL2, NRL3, and NRL5 in the upper layer and at NRL1, NRL3, and NRL5 in the lower layer. Net transports in the lower layer were about 0 Sv at NRL2 and 6 Sv (short record) at NRL4. Transport at NRL1 is not likely to be steered into the BoB by the SLD or large anticyclonic eddy. The current flows in the lower layer are not necessarily reflective of flows in the upper layer.

The current observations presented here suggest that upper-layer water from the southeastern Arabian Sea can enter the south-central BoB through steering of portions of the SMC by the SLD and large anticyclonic eddy during the summer monsoon. Water in the lower layer moves into the BoB throughout the year and appears to be less influenced by eddies and local winds.

Northward transport into the BoB appeared to be concentrated in the vicinity of NRL3.

Another reported route for water to move from the BoB to the Arabian Sea is through the EICC off Sri Lanka (e.g., Shetye et al. 1996; Wijesekera et al. 2015). Transports for the EICC have been estimated to be about 6.7 Sv from an ocean model (Shankar et al. 1996) and 7.7 Sv from hydrography (Shetye et al. 1996). These transports were estimated over a period of about 3 months during the northeast monsoon. Hence, the average outgoing transport over the entire year could be about 2 Sv, which is comparable to the average incoming transport computed at the moorings in the south-central BoB.

Gordon et al. (2016) described regional-scale water mass structures from CTD observations collected during November–December 2013 cruises, satellite sea surface temperature and salinity, and Argo temperature and salinity profiles. They reported that thermocline mesoscale features spread salty Arabian Sea Water under the highly stratified low-salinity upper layer. The mooring observations showed that the high-salinity water was carried by both mesoscale eddies and northward-moving currents. The mooring observations further showed that the warm, high-salinity, subsurface water entered the southern BoB during both winter and summer. Similar temperature–salinity features were found from CTD profiles (not shown), collected during December 2013, June 2014, and August 2015. The temperature–salinity properties of these water masses, with salinities larger than 35 psu, are consistent with Arabian Sea Water (e.g., Gordon et al. 2016). During summer months, Arabian Sea Water was found at all mooring sites and was associated with the SMC and SLD, while in winter the Arabian Sea Water was found at the western side of the mooring array. Wijesekera et al. (2015) reported that an approximately 100-km-wide, 1 m s^{-1} , northward-moving, subsurface-intensified current, located east of the EICC, carried Arabian Sea Water into the southern BoB during winter of 2013. The SMC transports Arabian Sea Water into the BoB, while the equatorial dynamics plays a role in wintertime transports. These observations are qualitatively consistent with numerical studies reported by Jensen et al. (2016), who found a persistent flow of high-salinity water from the equatorial Indian Ocean into the BoB during the northeast monsoon, although the salt transport is weaker than during the southwest monsoon.

11. Summary and conclusions

Long-term measurements of currents were made in the deep water in the south-central BoB, encompassing

a region 5° – 8° N, 85° – 89° E for the first time. Seasonal, intraseasonal, inertial, and tidal bands of currents and cyclonic and anticyclonic mesoscale eddies were found in the long-term record. Seasonal flow in the upper 200 m reversed with SW and NE monsoons. Currents were strongest during the SW monsoon with a maximum observed speed of 198 cm s^{-1} . The maximum observed speed during the NE monsoon was 132 cm s^{-1} . Averaged currents with periods longer than a month often exceeded 50 cm s^{-1} . During August 2014, the average velocity exceeded 70 cm s^{-1} at NRL3 (8° N, 86.5° E) in the upper 50 m of the water column. Velocities were typically much larger in the upper 200 m and often reversed directions at depth. Surface currents were not indicative of water movement at depth. Subsurface maximums in currents were common.

The seasonal cycle of SSHA closely followed the thermocline (20°C isotherm) displacement. Both 120-day, low-pass filtered SSHA and the 20°C isotherm moved westward at a speed of about 10 cm s^{-1} . Similar westward propagation was observed in the 20–120-day, bandpass-filtered SSHA, but the speed was about 21 cm s^{-1} , which is a factor of 2 bigger than that of the seasonal scale. It is likely that these westward-moving seasonal and intraseasonal fluctuations are related to Rossby waves as described in Subrahmanyam et al. (2001) and Girishkumar et al. (2011).

Multiple frequency bands of intraseasonal currents ranging from 10, 30, 50, and 60–70 days were found in the water column (within the 500-m observational window), and currents in excess of 25 cm s^{-1} were common in the upper 100 m. Currents below 200 m were weaker, but bursts of currents occurred somewhat intermittently throughout the record. Temperature fluctuations of ISO were also found in the water column, but fluctuations as large as $\pm 3^{\circ}\text{C}$ were limited to the main thermocline (50–150 m).

The major semidiurnal tidal constituent was M_2 , which had an amplitude of about 3 cm s^{-1} . Diurnal tides were weaker with maximum amplitudes of about 1 cm s^{-1} . Currents at frequencies lower than the inertial frequency (periods > 6 days) contributed over 60% of the total current energy in the upper 500 m, reaching a maximum contribution near 50-m depth and then increasing contribution with depth below 200 m.

Multiple mesoscale features including the SLD and an anticyclonic eddy were observed by the mooring array. In general, both eddies were similar in size and had similar magnitudes of SSHA. The SLD was found when the wind stress curl east of Sri Lanka was positive. The SLD had a negative 20-cm SSHA and was about 200–300 km in size with a cold temperature core of about 25°C . The relative vorticity of the SLD was $(0.2\text{--}0.3)f_{6.5\text{N}}$,

and the associated upwelling velocity was $3\text{--}4\text{ m day}^{-1}$ at 25 m. The anticyclonic eddy found south and southwest of the SLD had a positive 20-cm SSHA with a relative vorticity of about $-(0.5\text{--}0.8)f_{6.5N}$ and a downwelling velocity of $3\text{--}4\text{ m day}^{-1}$ at 25 m. Unlike the SLD, the anticyclonic eddy had high relative vorticity.

Currents from the SLD and an anticyclonic eddy during the summer monsoon appeared to facilitate water transport into the BoB through interactions with the summer and winter monsoon currents. An estimate of the average northward transport of water into the BoB over the measurement period is about 2 Sv. During summer 2014, the northward average transport into the BoB is estimated as 8 Sv over a 50-day period. These transport estimates assumed a current width of 100 km and could be larger for wider currents, which have been observed in the BoB. The transports in the upper layer appear to be steered by the SLD and large anticyclonic eddy. Northward transports in the lower layer appear to be less affected by the eddies. Much of the northward transport into the BoB in the upper layer appeared to be associated with the summer monsoon while northward transport in the lower layer occurred throughout the year at a magnitude comparable to the transport into the upper layer. Hence, the south-central BoB provides a pathway for transport of heat and salt into the interior BoB throughout the entire year. These may be the first set of observations, and certainly the first long-term observations, of the pathway for water transport into the south-central BoB through both a near-surface layer (0 to 200 m) and a deep, subsurface layer (200 to 500 m).

Acknowledgments. This work was sponsored by the United States Office of Naval Research (ONR) in an ONR Departmental Research Initiative (DRI), Air–Sea Interactions in Northern Indian Ocean (ASIRI), and a Naval Research Laboratory project, Effects of Bay of Bengal Freshwater Flux on Indian Ocean Monsoon (EBOB). HJSF and SUPJ were funded by the ONR Grants N00014-13-1-0199 and N00014-14-1-0279. Special thanks to Mr. Andrew Quaid, Mr. Steven Sova, and Mr. Justin Brodersen for their extraordinary efforts for preparation, deployment, and recovery of the moorings. Assistance provided by Mr. Praneeth Gunawardena and his colleagues of Maritime Agencies, Hayleys Group in Sri Lanka, Mr. David Anderson of ProteQ, Reston, VA, and the crew of the R/V *Roger Revelle* was greatly appreciated.

REFERENCES

- Bhat, G. S., and Coauthors, 2001: BOBMEX—The Bay of Bengal Monsoon Experiment. *Bull. Amer. Meteor. Soc.*, **82**, 2217–2243, doi:10.1175/1520-0477(2001)082<2217:BTBOBM>2.3.CO;2.
- Chen, S., and Coauthors, 2003: COAMPS version 3 model description—general theory and equations. Naval Research Laboratory Publication NRL/PU/7500–03-448, 143 pp. [Available online at <http://www.nrlmry.navy.mil/coamps-web/web/docs>.]
- Cheng, X., S. P. Xie, J. P. McCreary, Y. Qi, and Y. Du, 2013: Intraseasonal variability of sea surface height in the Bay of Bengal. *J. Geophys. Res. Oceans*, **118**, 816–830, doi:10.1002/jgrc.20075.
- de Vos, A., C. B. Pattiaratchi, and E. M. S. Wijeratne, 2014: Surface circulation and upwelling patterns around Sri Lanka. *Bio-geosciences*, **11**, 5909–5930, doi:10.5194/bg-11-5909-2014.
- Eigenheer, A., and D. Quadfasel, 2000: Seasonal variability of the Bay of Bengal circulation inferred from TOPEX/Poseidon altimetry. *J. Geophys. Res.*, **105**, 3243–3252, doi:10.1029/1999JC900291.
- Girishkumar, M. S., M. Ravichandran, M. J. McPhaden, and R. R. Rao, 2011: Intraseasonal variability in barrier layer thickness in the south central Bay of Bengal. *J. Geophys. Res.*, **116**, C03009, doi:10.1029/2010JC006657.
- Gordon, A. L., E. L. Shroyer, A. Mahadevan, D. Sengupta, and M. Freilich, 2016: Bay of Bengal: 2013 northeast monsoon upper-ocean circulation. *Oceanography*, **29**, 82–91, doi:10.5670/oceanog.2016.41.
- Hacker, P., E. Firing, and J. Hummon, 1998: Bay of Bengal currents during the northeast monsoon. *Geophys. Res. Lett.*, **25**, 2769–2772, doi:10.1029/98GL52115.
- Han, W., 2005: Origins and dynamics of the 90-day and 30–60-day variations in the equatorial Indian Ocean. *J. Phys. Oceanogr.*, **35**, 708–728, doi:10.1175/JPO2725.1.
- Iskandar, I., and M. J. McPhaden, 2011: Dynamics of wind-forced intraseasonal zonal current variations in the equatorial Indian Ocean. *J. Geophys. Res.*, **116**, C06019, doi:10.1029/2010JC006864.
- Jensen, T. G., 2001: Arabian Sea and Bay of Bengal exchange of salt and tracers in an ocean model. *Geophys. Res. Lett.*, **28**, 3967–3970, doi:10.1029/2001GL013422.
- , 2003: Cross-equatorial pathways of salt and tracers from the northern Indian Ocean: Modelling results. *Deep-Sea Res. II*, **50**, 2111–2128, doi:10.1016/S0967-0645(03)00048-1.
- , H. W. Wijesekera, E. S. Nyadjro, P. Thoppil, J. Shriver, K. K. Sandeep, and V. Pant, 2016: Modeling salinity exchanges between the equatorial Indian Ocean and the Bay of Bengal. *Oceanography*, **29**, 92–101, doi:10.5670/oceanog.2016.42.
- Kumar, P. S., M. Nuncio, N. Ramaiah, S. Sardesai, J. Narvekar, F. Veronica, and T. P. Jane, 2007: Eddy-mediated biological productivity in the Bay of Bengal during fall and spring intermonsoons. *Deep-Sea Res. I*, **54**, 1619–1640, doi:10.1016/j.dsr.2007.06.002.
- Lee, C. M., and Coauthors, 2016: Collaborative observations of boundary currents, water mass variability, and monsoon response in the southern Bay of Bengal. *Oceanography*, **29**, 102–111, doi:10.5670/oceanog.2016.43.
- Liu, P. C., and G. S. Miller, 1996: Wavelet transforms and ocean current data analysis. *J. Atmos. Oceanic Technol.*, **13**, 1090–1099, doi:10.1175/1520-0426(1996)013<1090:WTAOCD>2.0.CO;2.
- Lucas, A. J., and Coauthors, 2014: From monsoons to mixing: The multi-scale mosaic of air-sea interactions in the Bay of Bengal. *Eos, Trans. Amer. Geophys. Union*, **95**, 269–276, doi:10.1002/2014EO300001.
- McCreary, J. P., W. Han, D. Shankar, and S. R. Shetye, 1996: Dynamics of the East India Coastal Current: 2. Numerical solutions. *J. Geophys. Res.*, **101**, 13 993–14 010, doi:10.1029/96JC00560.

- McPhaden, M. J., and Coauthors, 2009: RAMA: The Research Moored Array for African-Asian-Australian Monsoon Analysis and Prediction. *Bull. Amer. Meteor. Soc.*, **90**, 459–480, doi:10.1175/2008BAMS2608.1.
- Moum, J. N., and J. D. Nash, 2009: Measurements of mixing on an equatorial ocean mooring. *J. Atmos. Oceanic Technol.*, **26**, 317–336, doi:10.1175/2008JTECHO617.1.
- Mukherjee, A., and Coauthors, 2014: Observed seasonal and intraseasonal variability of the East India Coastal Current on the continental slope. *J. Earth Syst. Sci.*, **123**, 1197–1232, doi:10.1007/s12040-014-0471-7.
- Murty, V. S. N., Y. V. B. Sarma, D. P. Rao, and C. S. Murty, 1992: Water characteristics, mixing and circulation in the Bay of Bengal during southwest monsoon. *J. Mar. Res.*, **50**, 207–228, doi:10.1357/002224092784797700.
- , —, and —, 1996: Variability of the oceanic boundary layer characteristics in the northern Bay of Bengal during MONTBLEX-90. *Proc. Indian Acad. Sci. (Earth Planet. Sci.)*, **105**, 41–61, doi:10.1007/BF02880758.
- Potemra, J. T., M. E. Luther, and J. J. O'Brien, 1991: The seasonal circulation of the upper ocean in the Bay of Bengal. *J. Geophys. Res.*, **96**, 12 667–12 683, doi:10.1029/91JC01045.
- Rao, R. R., M. S. Girish Kumar, M. Ravichandran, A. R. Rao, V. V. Gopalakrishna, and P. Thadathil, 2010: Interannual variability of Kelvin wave propagation in the wave guides of the equatorial Indian Ocean, the coastal Bay of Bengal and the southeastern Arabian Sea during 1993–2006. *Deep-Sea Res. I*, **57**, 1–13, doi:10.1016/j.dsr.2009.10.008.
- Rao, S. A., and Coauthors, 2011: Modulation of SST, SSS over northern Bay of Bengal on ISO time scale. *J. Geophys. Res.*, **116**, C09026, doi:10.1029/2010JC006804.
- Schott, F. A., and J. P. McCreary, 2001: The monsoon circulation of the Indian Ocean. *Prog. Oceanogr.*, **51**, 1–123, doi:10.1016/S0079-6611(01)00083-0.
- , J. Reppin, and J. Fisher, 1994: Currents and transports of the Monsoon Current south of Sri Lanka. *J. Geophys. Res.*, **99**, 25 127–25 141, doi:10.1029/94JC02216.
- , M. Dengler, and R. Schoenefeldt, 2002: The shallow overturning circulation of the Indian Ocean. *Prog. Oceanogr.*, **53**, 57–103, doi:10.1016/S0079-6611(02)00039-3.
- Shankar, D., J. P. McCreary, W. Han, and S. R. Shetye, 1996: Dynamics of the East India Coastal Current: 1. Analytical solutions forced by interior Ekman pumping and local alongshore winds. *J. Geophys. Res.*, **101**, 13 975–13 991, doi:10.1029/96JC00559.
- , P. N. Vinayachandran, and A. S. Unnikrishnan, 2002: The monsoon currents in the north Indian Ocean. *Prog. Oceanogr.*, **52**, 63–120, doi:10.1016/S0079-6611(02)00024-1.
- Shenoi, S. S. C., D. Shankar, and S. R. Shetye, 2002: Differences in heat budgets of the near-surface Arabian Sea and Bay of Bengal: Implications for the summer monsoon. *J. Geophys. Res.*, **107**, 3052, doi:10.1029/2000JC000679.
- Shetye, S. R., A. D. Gouveia, S. S. C. Shenoi, D. Sundar, G. S. Michael, and G. Nampoothiri, 1993: The western boundary current of the seasonal subtropical gyre in the Bay of Bengal. *J. Geophys. Res.*, **98**, 945–954, doi:10.1029/92JC02070.
- , —, D. Shankar, S. S. C. Shenoi, P. N. Vinayachandran, D. Sundar, G. S. Michael, and G. Nampoothiri, 1996: Hydrography and circulation in the western Bay of Bengal during the northeast monsoon. *J. Geophys. Res.*, **101**, 14 011–14 025, doi:10.1029/95JC03307.
- Somayajulu, Y. K., V. S. N. Murty, and Y. V. B. Sarma, 2003: Seasonal and inter-annual variability of surface circulation in the Bay of Bengal from TOPEX/Poseidon altimetry. *Deep-Sea Res. II*, **50**, 867–880, doi:10.1016/S0967-0645(02)00610-0.
- Subrahmanyam, B., I. S. Robinson, J. R. Blundell, and P. G. Challenor, 2001: Indian Ocean Rossby waves observed in TOPEX/POSEIDON altimeter data and in model simulations. *Int. J. Remote Sens.*, **22**, 141–167, doi:10.1080/014311601750038893.
- Suresh, I., J. Vialard, M. Lengaigne, W. Han, J. McCreary, F. Durand, and P. M. Muraleedharan, 2013: Origins of wind-driven intraseasonal sea level variations in the north Indian Ocean coastal waveguide. *Geophys. Res. Lett.*, **40**, 5740–5744, doi:10.1002/2013GL058312.
- Teague, W. J., H. W. Wijesekera, E. Jarosz, A. Lugo-Fernandez, and Z. R. Hallock, 2014: Wavelet analysis of near-inertial currents at the East Flower Garden Bank. *Cont. Shelf Res.*, **88**, 47–60, doi:10.1016/j.csr.2014.06.013.
- Vialard, J., S. S. C. Shenoi, J. P. McCreary, D. Shankar, F. Durand, V. Fernando, and S. R. Shetye, 2009: Intraseasonal response of the northern Indian Ocean coastal waveguide to the Madden-Julian oscillation. *Geophys. Res. Lett.*, **36**, L14606, doi:10.1029/2009GL038450.
- Vinayachandran, P. N., and T. Yamagata, 1998: Monsoon response of the sea around Sri Lanka: Generation of thermal domes and anticyclonic vortices. *J. Phys. Oceanogr.*, **28**, 1946–1960, doi:10.1175/1520-0485(1998)028<1946:MR0TSA>2.0.CO;2.
- , Y. Masurnoto, T. Mikawa, and T. Yamagata, 1999: Intrusion of the Southwest Monsoon Current into the Bay of Bengal. *J. Geophys. Res.*, **104**, 11 077–11 085, doi:10.1029/1999JC900035.
- , V. S. N. Murty, and V. R. Babu, 2002: Observations of barrier layer formation in the Bay of Bengal during summer monsoon. *J. Geophys. Res.*, **107**, 8018, doi:10.1029/2001JC000831.
- , D. Shankar, S. Vernekar, K. K. Sandeep, P. Amol, C. P. Neema, and A. Chatterjee, 2013: A summer monsoon pump to keep the Bay of Bengal salty. *Geophys. Res. Lett.*, **40**, 1777–1782, doi:10.1002/grl.50274.
- Webster, P. J., and Coauthors, 2002: The JASMINE pilot study. *Bull. Amer. Meteor. Soc.*, **83**, 1603–1630, doi:10.1175/BAMS-83-11-1603.
- Wijesekera, H. W., D. W. Wang, W. J. Teague, E. Jarosz, W. E. Rogers, D. B. Fribance, and J. N. Moum, 2013: Surface wave effects on high-frequency currents over a shelf edge bank. *J. Phys. Oceanogr.*, **43**, 1627–1647, doi:10.1175/JPO-D-12-0197.1.
- , and Coauthors, 2015: Southern Bay of Bengal currents and salinity intrusions during the northeast monsoon. *J. Geophys. Res. Oceans*, **120**, 6897–6913, doi:10.1002/2015JC010744.
- , and Coauthors, 2016a: Observations of currents over the deep southern Bay of Bengal—With a little luck. *Oceanography*, **29**, 112–123, doi:10.5670/oceanog.2016.44.
- , and Coauthors, 2016b: ASIRI: An ocean-atmosphere initiative for Bay of Bengal. *Bull. Amer. Meteor. Soc.*, doi:10.1175/BAMS-D-14-00197.1, in press.
- Wyrtki, K., 1973: An equatorial jet in the Indian Ocean. *Science*, **181**, 262–264, doi:10.1126/science.181.4096.262.
- Yu, L., 2003: Variability of the depth of the 20°C isotherm along 6°N in the Bay of Bengal: Its response to remote and local forcing and its relation to satellite SSH variability. *Deep-Sea Res. II*, **50**, 2285–2304, doi:10.1016/S0967-0645(03)00057-2.